Received: 27 March 2019 | Revised: 22 September 2019 | Accepted: 23 September 2019

DOI: 10.1111/bre.12410

ORIGINAL ARTICLE

Basin Research IAS EAGE WILEY

Architecture of growth basins in a tidally influenced, prodelta to delta-front setting: The Triassic succession of Kvalpynten, East Svalbard

Aleksandra Smyrak-Sikora[1,2] | **Per Terje Osmundsen**[3,4] | **Alvar Braathen**[1,4] | **Kei Ogata**[5] | **Ingrid Anell**[4] | **Mark J. Mulrooney**[4] | **Valentin Zuchuat**[4]

[1]Department of Arctic Geology, University Centre in Svalbard, Longyearbyen, Norway

[2]Department of Earth Science, University of Bergen, Bergen, Norway

[3]Department of Geoscience and Petroleum, Norwegian University of Science and Technology, Trondheim, Norway

[4]Department of Geosciences, University of Oslo, Oslo, Norway

[5]Faculty of Science, Geology and Geochemistry Cluster, VU Amsterdam, Amsterdam, The Netherlands

Correspondence
Aleksandra Smyrak-Sikora, Department of Arctic Geology, University Centre in Svalbard, Longyearbyen, Norway.
Email: aleksandras@unis.no

Funding information
Norges Forskningsråd, Grant/Award Number: grant 234152/E30

Abstract

World-class examples of fault-controlled growth basins with associated syn-kinematic sedimentary fill are developed in Upper Triassic prodelta to delta-front deposits exposed at Kvalpynten, SW Edgeøya in East Svalbard. They are interpreted to have interacted with north-westerly progradation of a regional delta system. The syn-kinematic successions consist of 4 to 5 coarsening-upward units spanning from offshore mudstones to subtidal heterolithic bars and compound tidal dunes, which were blanketed by regional, post-kinematic sandstone sheets deposited as laterally continuous, subaqueous tidal dune fields. The rate of growth faulting is reflected in the distribution of accommodation, which governs sedimentary architecture and stacking patterns within the coarsening-upward units. Fully compartmentalized basins (12, 200–800 m wide and c. 150 m high grabens and half grabens) are characterized by syn-kinematic sedimentary infill. These grabens and half-grabens are separated by 60–150 m high horsts composed of pro-delta to distal delta-front mudstones. Grabens host tabular tidal dunes (sandwaves), whereas half-grabens bound by listric faults (mainly south-dipping) consist of wedge-shaped, rotated strata with erosive boundaries proximal to the uplifted fault block crests. Heterolithic tidal bars (sand ridges) occur in narrow half-grabens, showing migration oblique to the faults, up the dipslope. Structureless sandstone wedges and localized subaqueous slumps that formed in response to collapse of the block crests were only documented in half-grabens. Late-kinematic deposition during the final stages of faulting occurred in partly compartmentalized basins, filled with variably thick sets of continuous sandstone belts (compound tidal dunes).

1 | INTRODUCTION

Syn-sedimentary growth faults are often associated with deltas discharging sediments into shallow seas, as recognized in: (a) foreland basins (Bhattacharya & Davies, 2001; Bouroullec et al., 2004; Braathen, Midtkandal, et al., 2018; Fielding, 2015; Shultz & Hubbard, 2005), (b) extensional basins (Martinsen, 1989; Wignall & Best, 2004), (c) epicontinental seas (Edwards, 1976; Nemec et al., 1988; Osmundsen, Braathen, Rød, & Hynne, 2014; Prestholm

& Walderhaug, 2000) and (d) in forearc basins (Zecchin, Massari, Mellere, & Prosser, 2004). Large systems of growth faults are also developed along continental margins, as observed in outcrops of NW Borneo (Back, Strozyk, Kukla, & Lambiase, 2008; Burhannudinnur & Morley, 1997; Morley, Back, Rensbergen, Crevello, & Lambiase, 2003; van der Zee & Urai, 2005) and in seismic data sets (Lopez, 1990; Weber, 1987). These growth fault systems dissect offshore organic-rich mudstones overlain by reservoir sandstones and are often associated with prolific petroleum systems (Caillet & Batiot, 2003; Weber, 1987). Recent seismic studies address large-scale 3D geometries and fault evolution (Fazlikhani, Back, Kukla, & Fossen, 2017; Hiscott, 2001; Tvedt, Rotevatn, Jackson, Fossen, & Gawthorpe, 2013), however, they miss details regarding distribution of sedimentary facies impacted by faulting.

Growth faults commonly appear listric on the seismic profiles and in outcrops, with an overall fault trend parallel to the palaeo-shelf margin or delta lobe slope (e.g. Back et al., 2008; Fielding, 2015). In a plan view they tend to show scoop or cuspate shapes (e.g. Braathen, Midtkandal, et al., 2018; Wignall & Best, 2004). Growth faults often initiate and evolve due to gravitational instability of a slope and/or loading of thick sandstone succession accumulated over a mobile substrate, that is salt or shale (e.g. Garfunkel, 1984; Winker & Edwards, 1983), differential compaction (Back & Morley, 2016; Bruce, 1973; Carver, 1968; Taylor, Nicol, & Walsh, 2008), fluid escape and shale expulsion (Van Rensbergen & Morley, 2000). A collapse above rising salt diapirs (Ings & Beaumont, 2010; Tvedt, Rotevatn, & Jackson, 2016) or shale diapirs (e.g. Morley & Guerin, 1996; Ocamb, 1961) can also induce growth faulting. Growth faulting can be spontaneous or be triggered by seismic events disturbing unstable and overpressured deposits (e.g. Garfunkel, 1984; Martinsen & Bakken, 1990; Martinsen, Lien, Walker, & Collinson, 2003; Nemec et al., 1988). The evolution of growth faults is often related to the lateral and vertical linkage of fault segments (e.g. Cartwright, Mansfield, & Trudgill, 1996; Rotevatn & Jackson, 2014; Rykkelid & Fossen, 2002; Serck & Braathen, 2019; Tvedt et al., 2013; Walsh, Bailey, Childs, Nicol, & Bonson, 2003). Field- and seismic-based studies and analogue modelling mainly show that extensional faulting tend to affect the delta top and upper delta front of the prograding deltaic system, whereas the lower delta front/prodelta can experience shortening and in some cases formation of gravity-induced deep water fold-and-thrust belts (e.g. Braathen, Midtkandal, et al., 2018; Ings & Beaumont, 2010; McClay, Dooley, & Lewis, 1998; Rouby et al., 2011; Winker & Edwards, 1983).

Syn-sedimentary architecture of fault-bounded basins in prograding delta deposits has been previously assessed through the study of exhumed Triassic strata onshore Svalbard on Edgeøya island (Figure 1a,b; e.g. Edwards, 1976; Osmundsen et al., 2014; Maher, Ogata, & Braathen, 2017; Ogata et al., 2018). The Kvalpynten faults are developed in a prodelta to lower delta front position within the distal part of a major deltaic system that prograded north-westwards across the Barents Shelf (Anell, Braathen, & Olaussen, 2014; Anell, Faleide, & Braathen, 2016; Glørstad-Clark, Birkeland, Nystuen, Faleide, & Midtkandal, 2011; Glørstad-Clark, Faleide, Lundschien, & Nystuen, 2010; Høy & Lundschien, 2011; Lundschien, Høy, & Mørk, 2014; Riis, Lundschien, Høy, Mørk, & Mørk, 2008; Worsley, 2008). The differential compaction in combination with reactivation of deep-seated faults have been suggested as a trigger mechanism for the Kvalpynten growth faults developed in lower delta front/prodelta position (Braathen, Midtkandal, et al., 2018; Maher et al., 2017; Ogata et al., 2018). Growth fault morphology impacted the topography of the basin floor, creating footwall highs and hanging wall lows (Braathen, Midtkandal, et al., 2018; Ogata et al., 2018), that defined compartments accumulating syn-kinematic deposits.

This study analyses the sedimentary architecture encountered in the growth-faulted, tidally-influenced, deltaic deposits of Kvalpynten, on Edgeøya, East Svalbard (Figure 1a,b). It specifically targets the growth units, which consists of Upper Triassic mudstones and sandstones (Braathen, Midtkandal, et al., 2018; Edwards, 1976; Maher et al., 2017; Ogata et al., 2018; Osmundsen et al., 2014). This study focuses on fault-controlled hanging wall accommodation, where sediments were funnelled into 200- to 800-m-wide depocentres, potentially extending over hundreds to thousands of metres. In such depocenters, slopes may change repeatedly and the substrate morphology may influence the distribution of tidal energy (e.g. Rossi et al., 2017). Erosion and sedimentation variations

Highlights

- The Triassic prodelta to delta-front succession in Kvalpynten (south-eastern Svalbard) is intersected by growth faults.
- Growth basins were filled with coarsening-upward units composed of prodelta mudstone, tidally-influenced, heterolithic strata and tidal dunes.
- Basin-fill reflect distinct rate and spatial distribution of creation of accommodation, which occur in: fully compartmentalized (a) half-grabens and (b) grabens, (c) late-kinematic accommodation witnessing ceasing faulting and (d) post-kinematic accommodation.
- Stacking of architectural elements within coarsening-upward growth units is controlled by the type of accommodation and sediment supply.

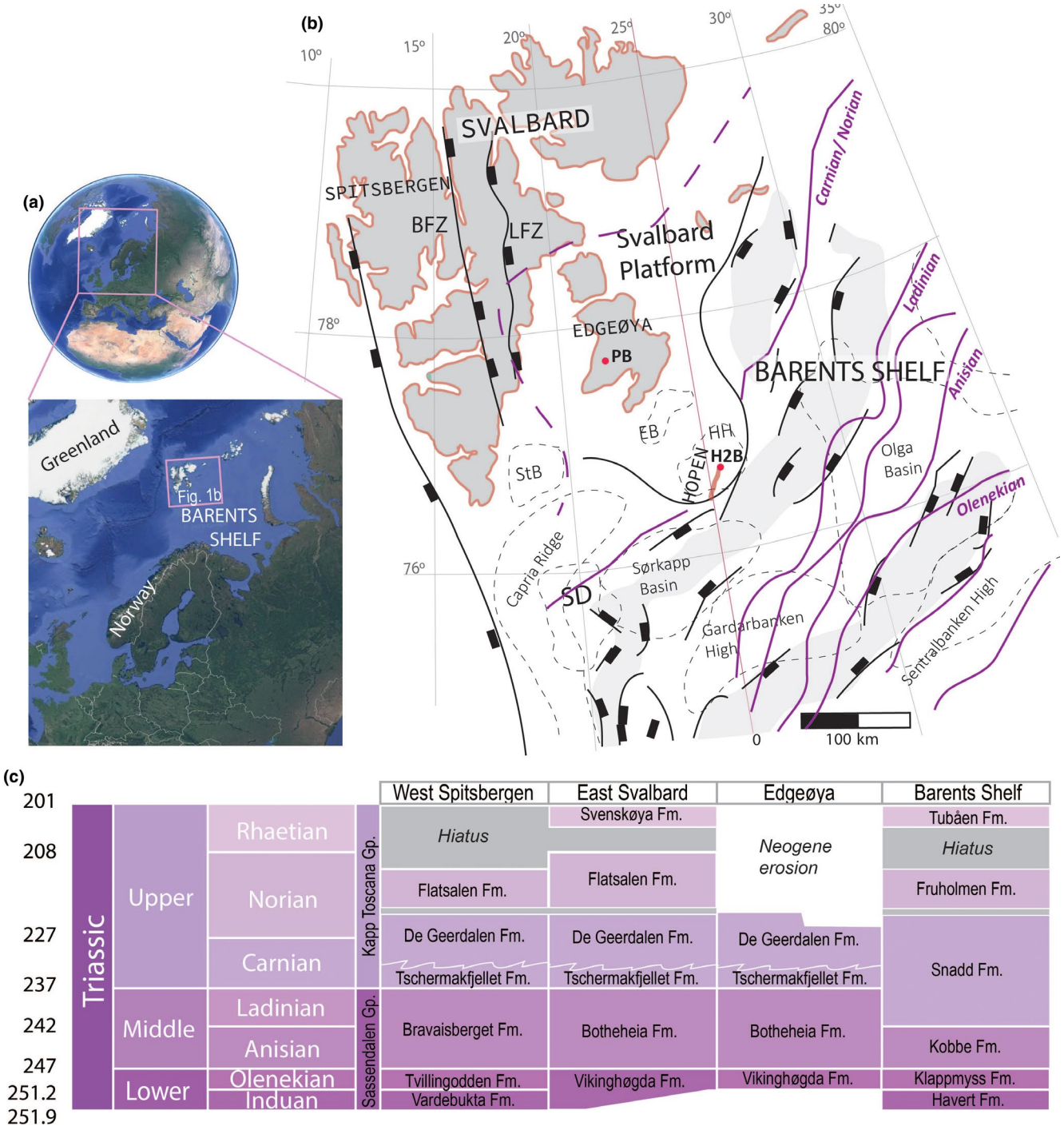

FIGURE 1 (a) Position of Svalbard on the Barents Shelf (Image sourced from https://earth.google.com) (b) Structural framework with upper Palaeozoic structures on the SW Barents Shelf. Palaeozoic rift basins are shaded with grey. Edgeøya island, Edgeøya Basin (EB) and Hopen High (HH) form the Svalbard Platform; Purple lines mark the position of clinoforms (deltaic platform edge in Anell et al., 2014) that prograded in the Triassic across the Barents Shelf (modified after Faleide et al., 2008 and Anell et al., 2014, 2016); Red dots show the position of Plurdalen borehole (PB) and Hopen 2 borehole (H2B); *SD* Sørkapp Depression, STB Storfjorden Basin; BFZ Billefjorden Fault Zone; LFZ Lomfjorden Fault Zone; (c) Triassic stratigraphy of Svalbard and Barents Shelf, grey boxes mark a hiatus; modified after Riis et al. (2008); Formations ages are from Vigran, Mangerud, Mørk, Worsley, & Hochuli, 2014; Paterson & Mangerud, 2015; Smelror, Larssen, Olaussen, Rømuld, & Robert, 2018; Rismyhr et al., 2019

within an environment with high tidal currents will impact the distribution of facies belts and facies stacking patterns, reflected in distinct sedimentary architectures. The main questions that this work will address are as follows:

- What kind of facies associations are deposited in the growth basins?
- How are the rates of fault-driven accommodation creation expressed in the sedimentary architecture?

- How did the basin geometry (i.e. symmetric vs. asymmetric growth-basins) impacted stacking of architectural elements?
- What controlled on development of coarsening-upward units?

The observations and interpretations reported in this study are relevant to studies in the Barents Sea region, as the Kvalpynten strata extend offshore (Anell, Braathen, Olaussen, & Osmundsen, 2013), where similar successions have been documented at sub-seismic to seismic scale (e.g. Mulrooney, Leutscher, & Braathen, 2017; Mulrooney et al., 2018; Serck, Faleide, Braathen, Kjølhamar, & Escalona, 2017). More broadly, this study provides insights into facies associations and facies architectures that can be expected in other growth-faulted deltaic successions systems around the world.

2 | GEOLOGICAL SETTING

The Svalbard archipelago represents the uplifted north-western region of the Barents Shelf (Figure 1a,b). Edgeøya is the third largest island of the archipelago. After tectonic instability in the Devonian (Braathen, Osmundsen, Maher, & Ganerød, 2018) and the subsequent Carboniferous to Middle Permian rifting (Ahlborn & Stemmerik, 2015; Braathen, Bælum, Maher, & Buckley, 2011; Johannessen & Steel, 1992; Smyrak-Sikora, Johannessen, Olaussen, Sandal, & Braathen, 2019), a fairly stable Svalbard Platform was established in the Late Permian (Figure 1b). Renewed mild and localized fault activity is reflected in thickness variations in Triassic deposits preserved both on- and offshore Svalbard's eastern flank (Anell et al., 2013; 2016; Ogata et al., 2018; Osmundsen et al., 2014). Tectonic instability during the Triassic is ascribed to far-field stresses transferred from the Uralian orogeny (Anell et al., 2013). Thickness variations of the Permian and Triassic deposits recorded between well data from Edgeøya and Hopen (Plurdalen and Hopen 2 wells Figure 1; Harland & Kelly, 1997) indicate a higher subsidence towards the southeast, towards Hopen Island and further towards the Barents Shelf (Figure 1b; Anell et al., 2016; Faleide, Gudlaugsson, & Jacquart, 1984; Fielding, 2015). The subsidence rates in the Barents Sea and in Svalbard decreased near the Triassic-Jurassic boundary (Rismyhr, Bjærke, Olaussen, Mulrooney, & Senger, 2019; Ryseth, 2014). A second phase of regional subsidence of the Svalbard Platform was initiated in the Middle Jurassic and lead to deposition of deeper marine sediments (Dypvik, Hakansson, & Heinberg, 2002; Koevoets, Hammer, Olaussen, Senger, & Smelror, 2019). Succeeding shallowing of the depositional environments is recorded by Lower Cretaceous deposits formed in response to uplift of the northern side of Svalbard (Gjelberg & Steel, 1995; Grundvåg et al., 2017; Grundvåg & Olaussen, 2017; Midtkandal & Nystuen, 2009; Midtkandal, Nystuen, Nagy, & Mørk, 2008; Olaussen et al., 2018). Exhumation of Triassic sedimentary rocks on Edgeøya resulted from Late Cretaceous uplift and associated magmatism, coupled with the establishment of a fold-and-thrust belt in the west of Svalbard during the Palaeogene, and isostatic post-glacial rebound, notably during the Holocene (Anell et al., 2013; Bergh, Maher, & Braathen, 2000; Braathen, Bergh, & Maher, 1999; Dallmann, Elvevold, Majka, & Piepjohn, 2015; Dimakis, Braathen, Faleide, Elverhøi, & Gudlaugsson, 1998; Faleide et al., 2008; 2017; Henriksen et al., 2011; Steel & Worsley, 1984; Worsley, 2008).

2.1 | Triassic sedimentary system on the Barents Shelf and the eastern Svalbard Platform

During the Triassic the Barents Shelf was a boreal, epicontinental basin with water depths in the range 200–400 m (Anell et al., 2014; 2016; Høy & Lundschien, 2011).The offshore shelfal deposits of the Lower Triassic were overlain by a mudstone-dominated deltaic successions sourced from the Uralides with minor additional sources from the Baltic shield to the south, and from Novaya Zemlya to the east (Figure 1b,c; Anell et al., 2014; ,2016, 2011; Eide, Klausen, Katkov, Suslova, & Helland-Hansen, 2017; Glørstad-Clark et al., 2010; Høy & Lundschien, 2011; Klausen, Ryseth, Helland-Hansen, Gawthorpe, & Laursen, 2015; Klausen et al., 2018; Lundschien et al., 2014; Riis et al., 2008; Worsley, 2008). In seismic data, this system is expressed as a set of northwest-prograding clinoforms (Anell et al., 2014; ,2016, 2011; Glørstad-Clark et al., 2010; Høy & Lundschien, 2011; Riis et al., 2008). On the Barents Shelf the delta top-sets consist of tidally-influenced distributary channel systems of the Snadd Formation (Figure 1c; Klausen et al., 2018; Riis et al., 2008).

The succession exposed on Edgeøya corresponds to the distal part of the upper Middle and Upper Triassic deltaic deposits (Glørstad-Clark et al., 2010; 2011; Høy & Lundschien, 2011; Mørk, Knarud, & Worsley, 1982) that onlap the Svalbard Platform (Figure 1b; Anell et al., 2014). The c. 80-m-thick shallow-marine, organic matter-rich mudstones of the Middle Triassic Botneheia Formation (Figure 1c; Krajewski, 2008) are capped by a 65- to 140-m-thick dark grey, mudstone-dominated, offshore to prodelta deposits of the Tschermakfjellet Formation (Figures 1c and 2). The prodelta deposits are overlain by 400-m-thick mixed sandstones and mudstones of the Carnian to Norian De Geerdalen Formation (Figures 1c and 2). This formation is characterized by shallowing-upward, tide-dominated deposits of delta-front to delta top (Flood, Nagy, & Winsnes, 1971; Haile et al., 2018; Klausen & Mørk, 2014; Lord, Johansen, Støen, & Mørk, 2017; Lord, Solvi, Klausen, & Mørk, 2014; Mørk

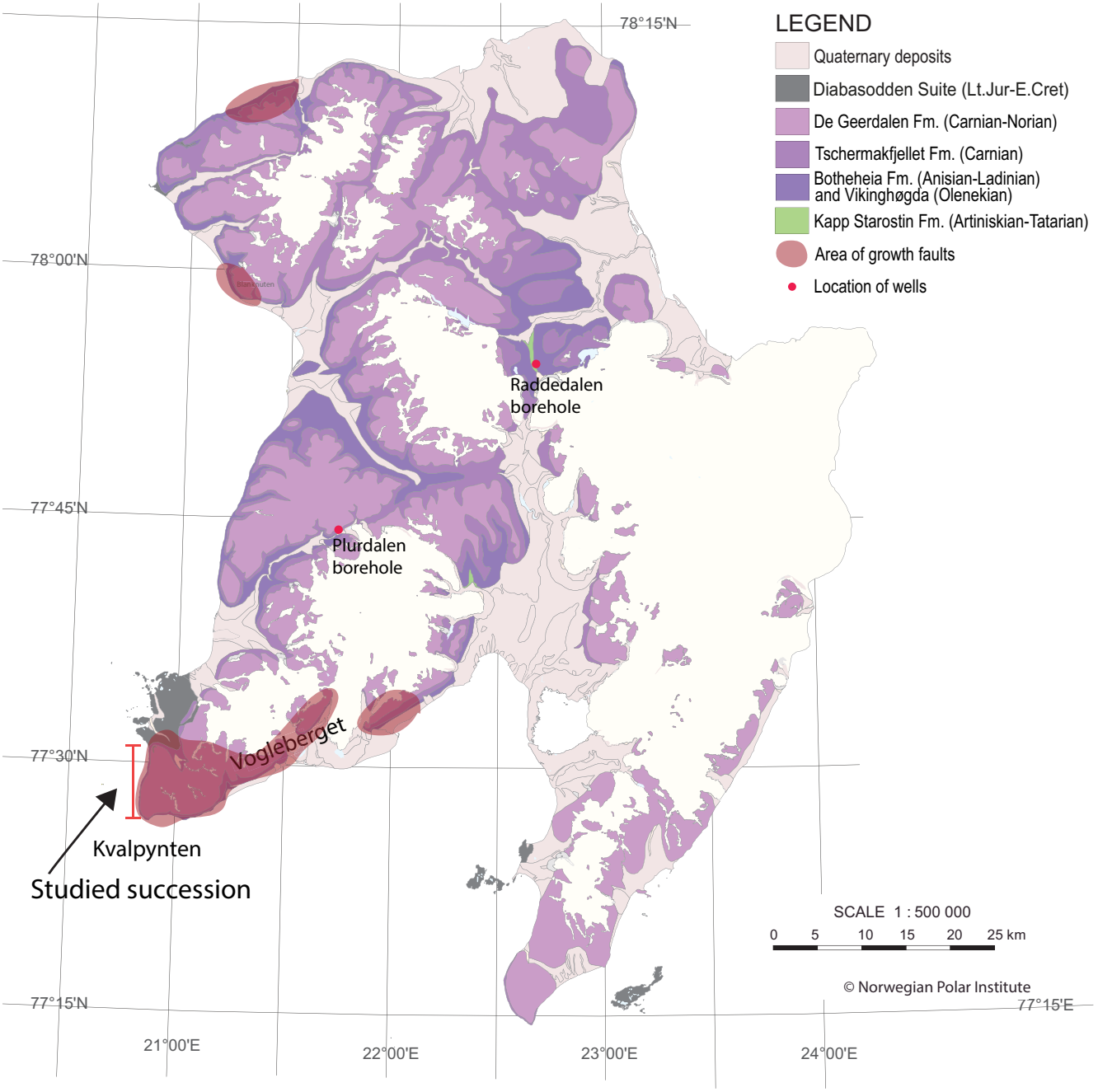

FIGURE 2 Geological map of eastern Svalbard with islands of Edgeøya and Barentsøya. The position of study area in Kvalpynten is outlined. Location of reported growth faults is marked in red

et al., 1982; Mørk, 1999; Riis et al., 2008; Rød, Hynne, & Mørk, 2014; Röhnert, 2016).

The Triassic succession on Edgeøya differs from the rest of Svalbard due to the occurrence of numerous rotated fault blocks. These structures were first identified by Edwards (1976) who interpreted them as growth faults related to the collapse of a southwards-prograding delta. Growth faults were recognized at Klinkhamaren, Øhmanfjellet and Tjuvfjordskarvet (Figure 2; Maher et al., 2017; Ogata et al., 2018; Osmundsen et al., 2014; Riis et al., 2008; Rød et al., 2014). The most spectacular outcrops of these faults are, however, located along the north-south oriented cliffs of the Kvalpynten peninsula, as shown in Figure 3.

2.2 | The Kvalpynten succession

Growth faults occur only in the lower half of the 9 km long and c. 350–400 m high Kvalpynten cliff. Growth faults that display tens to a hundred of metres offsets are mainly observed in deposits of the Tschermakfjellet and De Geerdalen formations (Figures 2 and 3; Edwards, 1976; Ogata et al., 2018; Osmundsen et al., 2014; Rød

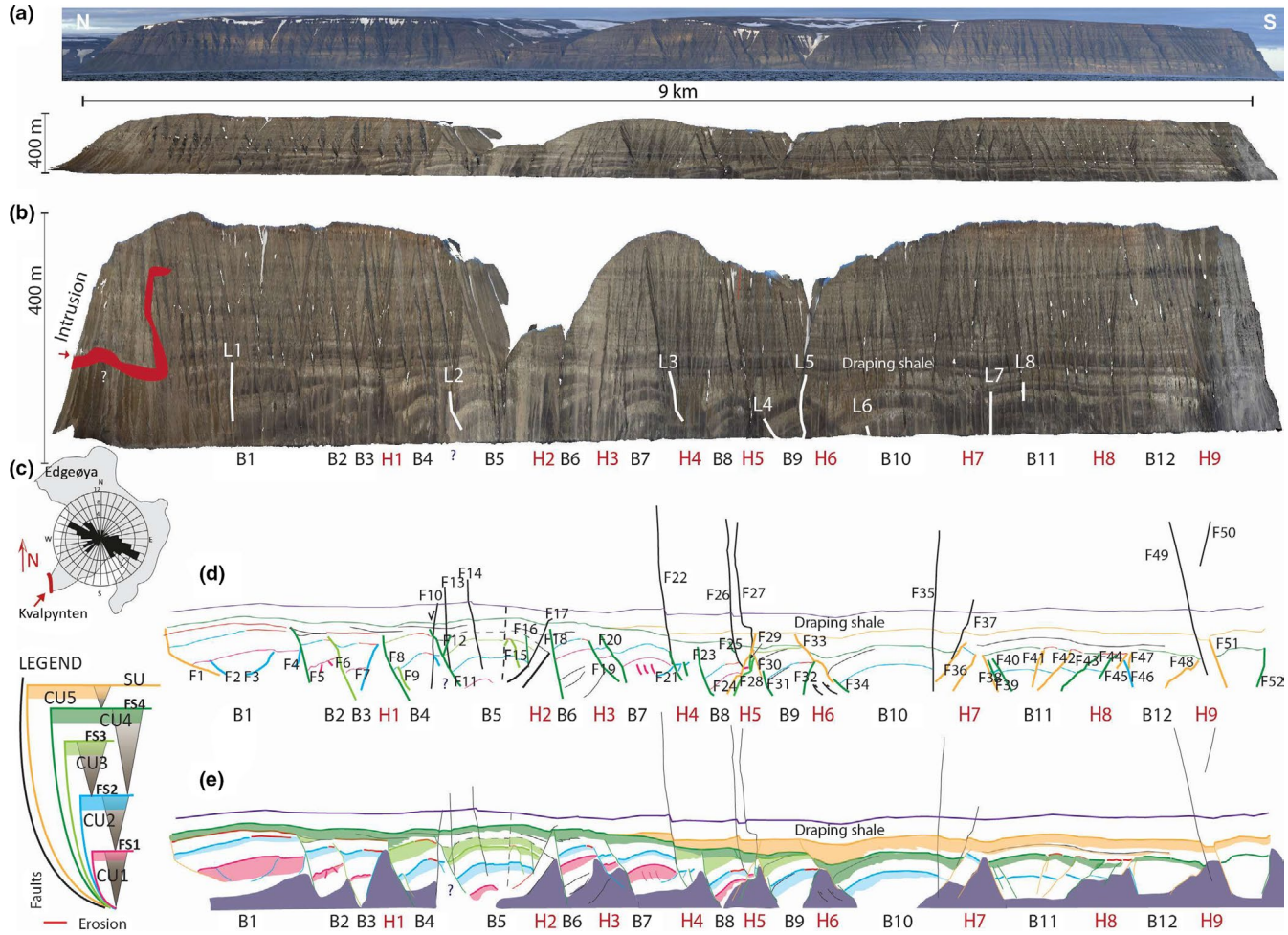

FIGURE 3 Transect of Kvalpynten with (a) photo mosaic (above) and photogrammetric outcrop model (below) of the 9-km-long and ca 400-m-high cliffs; Location in Figure 2 (b) vertically exaggerated by four photogrammetric outcrop model of Kvalpynten interpreted in LIME, presenting the position of nine horsts (H1-H9) and 12 basins (B1-B12), sedimentary logs (L1-L8) and Cretaceous intrusion (in red); (c) plot showing orientation of strike of extensional faults (d) Position of 52 extensional faults along the vertically exaggerated model; (e) Distribution of CUs 1–5 along the vertically exaggerated model with colours marking the position of upper, sandstone-dominated parts of CUs. FS: flooding surface; SAES: sub-aerially exposed surface

et al., 2014). The horsts consist of dark mudstone of the Botneheia and Tschermakfjellet formations (Figure 1c), exposing in places complex internal structures. These structures include numerous extensional faults and some minor thrust faults, the latter of which form gentle anticlinal stacks (Ogata et al., 2018). These minor structures likely represent some local shortening in the lower delta front/prodelta and challenge the mapping of the top of the Botneheia Formation.

The growth basin-fill is sandwiched between the near top of the Botneheia Formation and a flat-lying, 25- to 40-m thick, intra De Geerdalen Formation interval composed of dark mudstone, herein called the draping shale after Osmundsen et al. (2014; Figure 3a,b). The draping shale blankets the upper part of fault-related relief and serves as a marker bed (Figure 3e). It represents the boundary between two very different depositional and structural settings. The draping shale is overlain by c. 150- to 200-m thick, paralic deposits of the De Geerdalen Formation (Edwards, 1976; Haile et al., 2018; Klausen & Mørk, 2014; Lord et al., 2014; Mørk et al., 1982; 1999; Osmundsen et al., 2014; Riis et al., 2008; Rød et al., 2014; Röhnert, 2016). Some of the larger fluvial or fluvio-marine channels seen in the upper part of the Edgeøya outcrop probably represent deposition on a delta plain.

Compilations of fault orientations recorded in Kvalpynten show that the majority of faults strike west-northwest and east-northeast; they dip southerly, and are either planar or gently to strongly listric (Figure 3c; Anell et al., 2013; Ogata et al., 2018; Osmundsen et al., 2014). Associated fault striations/corrugations show dip-slip kinematics with subordinate oblique-slip. Accordingly, the fault system has an overall down-to-the-south orientation, reflecting north to north-northeast and south to

south-southwest extension (Maher et al., 2017; Ogata et al., 2018; Osmundsen et al., 2014). Detailed analysis of the faults demonstrates a transition from hydroplastic to brittle shearing/faulting (Maher et al., 2017; Ogata et al., 2018). The Edgeøya cliff sections show that the main phase of faulting terminates below the draping shale. The latter is overlain by a post-kinematic unit, which shows occasional dm to m scale, steep, planar faulting (Ogata et al., 2018; Osmundsen et al., 2014). Pervious interpretation of the faulting advocates thin-skinned faulting, interacting with deeply rooted faults, which have been interpreted in seismic sections from the adjacent offshore areas (Anell et al., 2013). In the study area, the basal detachment for the listric faults is located near—or at the top of the Botneheia Formation (Ogata et al., 2018).

3 | DATA SETS AND METHODS

To date, published work on the steep, 9-km-long and c. 350- to 400-m-high Kvalpynten cliff succession has been based mainly on photographic analysis (Edwards, 1976; Osmundsen et al., 2014) supplemented with some field observations (Høy & Lundschien, 2011; Osmundsen et al., 2014; Riis et al., 2008; Rød et al., 2014). Eight sedimentary sections representing a total of 680 m were measured in 1:50 scale during field campaigns in 2012, 2013 and 2014 (Indicated with logs L1-L8 marked in Figure 3b; Appendices S1–S4). These sections were collected from seven of 12 identified fault-bounded basins and correspond to the only accessible localities on these extremely steep exposed cliffs. The N–S striking outcrop is oriented at 60–70 degrees to the average WNW-ESE striking faults, offering high-angle, almost perpendicular cross sections through many half-graben and graben structures. The presented data set consists of sedimentary logs, outcrop photographs and palaeo-current measurements complemented by a photogrammetric outcrop model. Standard techniques in lithofacies analysis and architectural-element analysis (Walker, 1992) were used in order to interpret various depositional settings.

Analysis of the basin geometries and associated sedimentary-structural architecture was performed using a photogrammetric outcrop model (Figure 3). The photogrammetric model covers nearly 45 km of cliff-face around southern Edgeøya; in this study, only the c. 9-km-long N-S oriented Kvalpynten section has been analysed. The photogrammetric model was created applying the Structure from Motion (SfM) method (e.g. Chandler & Buckley, 2016) with GPS-oriented images from a Canon EOS 6D, collected from boats at a fixed distance from the cliffs. The resultant high-resolution digital elevation model was draped with the detailed outcrop photographs, which allowed examination of basin-fill geometries on scales of metres to hundreds of metres. LIME software (Buckley et al., 2019) was used for interpretation of the model. LIME allows for the measurement of distance between points, and the three-point determination of the strike and dip of surfaces. Faults were analysed in outcrops and mapped in LIME. The relative age of faulting was determined based on termination relationships with flooding surfaces traceable over large parts of the study area (FS1-4 in Figure 3d,e). In the field, sediment palaeo-transport direction throughout the succession was determined by measuring foresets in tabular and cross-stratified sandstones, asymmetric ripples, gutter casts, flutes and groove marks. Larger dunes/bars with clinoform foresets were also measured in LIME.

4 | RESULTS

In Kvalpynten, the growth faults segment the Triassic succession below the draping shale into 12, 200- to 800-m-wide half-grabens and grabens (basins B1-B12) and nine, 60- to 100-m-high horsts (H1-H9; Figure 3e). The half-graben and graben fills consist of prodelta and delta-front mudstones and sandstones of the Tschermakfjellet and lower part of the De Geerdalen formations. The lower boundary of the De Geerdalen Formation is defined as the base of first prominent sandstone unit that is located on top of the Tschermakfjellet Formation pro-delta mudstones (Mørk et al., 1999). In Kvalpynten this boundary is somewhat ambiguous and is variably expressed in different basins.

Along the north-south-trending Kvalpynten, 52 faults were mapped and analysed (Figure 3d). Detailed descriptions of the faults and corresponding analyses of the faulting evolution are provided in Maher et al. (2017) and Ogata et al. (2018) and will not be repeated here. Among the mapped faults, 31 are south-dipping and 21 are north-dipping (Figure 3d). They can be divided into three categories based on their relationships to adjacent basins:

(i) Twenty three mainly south-dipping listric growth faults with vertical offsets exceeding 100 m that bound teen half-grabens.
(ii) Nineteen planar, synthetic and antithetic growth faults with vertical offsets exceeding 60 m. Planar faults bound two, nearly symmetric grabens.
(iii) Teen, post-sedimentary planar faults, with up to 3 m vertical offset, truncating the entire exposed cliff succession.

Each of the 12 basins B1-B12 is filled with 3–5, 25- to 60-m thick, coarsening-upwards units (CUs 1–5) composed

TABLE 1 Summary of the lithostratigraphic facies

Facies	Description	Grain size	Structures	Bioturbation index (BI; Taylor & Goldring, 1993) and biogenic structures	Interpretation
A	Structureless, dark- to light grey sandstone, with soft sediment deformations	Fine- to medium-grained	The individual beds are 0.2 to 1.5 m thick, and amalgamated successions measure up to 17 m. The sandstone beds have a sharp or erosive lower boundary. The soft sediment structures exhibit dish-, flame- and loading structures, convolute bedding and internal folding commonly with overturned folds.	BI = 0	Soft sediment deformations can occur by liquidization impacting layers of contrasting density, often reflecting water escape and gravitational (slump) processes (Owen, 1987). The thicker amalgamated structureless beds can be linked to very rapid deposition from suspended load (GingrasPemberton & Smith, 2014) or fluidization of sands. The amalgamated beds are adjacent to the master fault of the half graben suggesting that the soft sediment structures are induced by fault movement (Seilacher, 1991).
B	Plane parallel-stratified sandstone	Very fine to upper fine-grained	The sedimentary structures are dominated by plane parallel stratification (PPS) organized in 0.1–2 m thick beds with a commonly sharp but occasionally also gradual lower boundary. Facies B might contain symmetric- and asymmetric ripples.	BI = 0, rarely 1	PPS is a characteristic sedimentary expression of burst-and-sweep traction that flows undergoing laminar upper-flow regime conditions, although PPS can still form at lower flow intensities when the sediment concentration in the water column is high (Ashley, 1990; Cheel & Middleton, 1986; Fielding, 2006; Massari, 1996; Pickering, Stow, Watson, & Hiscott, 1986).
C	Low-angle cross-bedded, dark- to light grey sandstone	Upper-very fine- to upper-fine-grained	Sandstone displays gently dipping cross-stratification, with a sharp to occasionally erosive lower boundary and the bed thickness of 0.3–2 m. Symmetric and asymmetric ripples may be developed occasionally.	BI = 0, rarely 1	Low-angle cross-bedding represents transitional bedform between dunes and upper plane beds as flow velocity increases or as sediment concentration in the water increases (Massari, 1996; Turner, 1981). The presence of scattered oscillation ripples illustrates the impact of minor wave activity.
D	Tangential cross-bedded, dark- to light grey - sandstone	Upper very fine to fine-grained	Sandstone beds exhibit sharp to erosive basal contact. Individual cross-stratified sets measure between 0.3 to 1 m. Amalgamated beds, i.e. co-sets can reach thickness of 7.5 m. Tabular cross-bedding with tangential foresets occur. Scattered rip-up clasts, asymmetrical ripples with mud drapes and symmetrical ripples occur locally. Rare fining upward trends.	BI = 0, rarely 1, Rare plant fragments	The amalgamated cross-bedding represents non-laminar unidirectional current migration of sinuous (3D) dunes (Allen, 1982; Venditti, Church, & Bennett, 2005). Plant remains indicate a proximal position of the deposits Mud drapes suggest slack water periods probably by tidal processes
E	Asymmetric ripple cross-stratified, dark- to light grey sandstone	Very fine- to fine-grained	Sandstone is dominated by asymmetrical ripple cross-stratification with climbing ripples occurring locally.	BI = 0, rarely 1	Asymmetric ripples are the product of downstream migrating bedforms within unidirectional non-laminar flow conditions (Allen, 1982). Climbing ripples reflect a sedimentation rate exceeding the bedform progradation speed (Ashley, Southard, & BooTHRoyD, 1982) resulting in a positive aggradation, which can reflect a sudden sediment input increase or a waning of the flow, or both.
F	Dark- to light grey sandstone with hummocky cross-stratification	Very fine- to upper-fine-grained	Sandstone is dominated by hummocky cross-stratification. Isolated dm-thick beds are characterized by a sharp to gradual lower boundary. Facies F sporadically display mud drapes.	BI = 0, rarely 1	Hummocky (HCS) cross-stratification is a result of combined unidirectional and wave-generated oscillatory currents. They are formed under extended wave periods and gentle oscillatory velocities and almost absent unidirectional flow (Dumas & Arnott, 2006). HCS are generally interpreted as a typical shallow water storm deposits as a result of storm-induced oscillatory current (Cheel & Leckie, 1993; Jelby, Grundvåg, Helland-Hansen, Olaussen, & Stemmerik, 2017).

(Continues)

TABLE 1 (Continued)

Facies	Description	Grain size	Structures	Bioturbation index (BI; Taylor & Goldring, 1993) and biogenic structures	Interpretation
G	Dark- to light grey sandstone, with symmetric ripple cross-stratification	Very fine- to fine-grained	Sandstone is dominated by symmetric ripple cross-stratification. Isolated dm-thick beds are characterized by a sharp to gradual lower boundary. Sporadically displaying mud drapes.	BI = 0, rarely 1	Symmetric ripples are a product of the oscillatory wave movement and are generally interpreted as upper shoreface deposits (Allen, 1982; Basilici, 1997).
H	Dark- to light grey, heterolithic sandstone with flaser bedding	Very fine- to fine-grained	Sandstone is dominated by symmetrical and asymmetrical ripple cross-stratification that forms individual beds or uppermost interval in upward coarsening strata from Facies K into Facies H. Scattered mud lenses, mud drapes, rip-up clasts.	BI = 0, rarely 1	Heterolithic deposits likely produced by waxing-waning tidal currents within a mixed mud-sand-rich environment (Baas, Best, & Peakall, 2016).
I	Heterolithic silt- and sandstone (dark- to light grey) with wavy bedding	Silt and very fine- to fine-grained sand	Laminated to undulated interbedded sandstone and siltstone siltstone Facies I is commonly found as individual beds or in coarsening upward intervals from Facies K into Facies I/H. The sandstone beds are characterized by symmetric ripple cross-stratification and scattered rip-up clasts. Occasional thickening-thinning rhythmicity of the beds is observed.	BI = 0, rarely 1	Heterolithic deposits produced by a rapid flow deceleration and/or expansion within a mixed mud-sand-rich environment (Baas et al., 2016). Rhythmicity interpreted as a response to cyclic waxing-waning tidal current over the area, such as neap-spring tidal cycles (Visser, 1980).
J	Heterolithic dark grey mud- to siltstone with lenticular bedding	Silt and very fine- to fine-grained sand	Light grey sandstone lenses occur within a laminated to undulating muddy to silty dark grey matrix. The sandstone lenses are often characterized by uni- and bidirectional-asymmetrical ripple cross-stratification. Commonly developed as individual beds or fine-grained intervals within an upward coarsening succession from Facies K into Facies I/H.	BI = 0, rarely 1	Heterolithic deposits produced by a rapid flow deceleration and/or expansion within a mixed mud-sand-rich environment (Baas et al., 2016). Bidirectional-current ripples suggest a certain degree of tidal reworking.
K	Laminated (platy), dark grey to grey mudstone and siltstone	Clay and silt	Laminated to undulating mud- to siltstone with thin mm to 1–2 cm thick, planar to wavy laminas and lenses of very fine sandstone. These sediments are heavily altered at the outcrop and break-up as chips. Sparse occurrence of current ripples.	BI = 0–2	The homogenous mud- and siltstone suggest deposition from suspension within a low-energy environment, as a result of hypopycnal flows. The planar and ripple laminated sandstone laminas and lenses suggest more rapid gravity deposits probably from hyperpycnal flows (Potter, Maynard, & Depetris, 2005).

of mudstone, heterolithic and sandstones. CUs 1–5 have been mapped along the photogrammetric model (Figure 3e). In total, 12 sedimentary lithofacies can be identified (Facies A-L; Table 1; see also Appendices S5 and S6). The lithofacies are in turn grouped into four facies associations, FA1-4 (Figures 4 and 5), which have been used for depositional environment interpretation. These facies associations are as follows: FA1: Prodelta to distal delta front deposits, FA2: tidally-influenced heteroliths, FA3: tidally-reworked sandstone dunes, and FA4: mass-flow sandstone deposits. Each CU includes of 2–4 facies associations.

4.1 | Facies Associations

4.1.1 | FA1: prodelta to distal delta front deposits

Description

FA1 is composed of 2- to 20-m thick, mudstone-dominated intervals (Facies K; Table 1) with very fine to fine-grained, structureless, 1-dm to 1-m thick sandstone beds (Facies A). In the lowermost part of the studied succession (CU1), the lower boundary of FA1 is expressed as a gradual transition

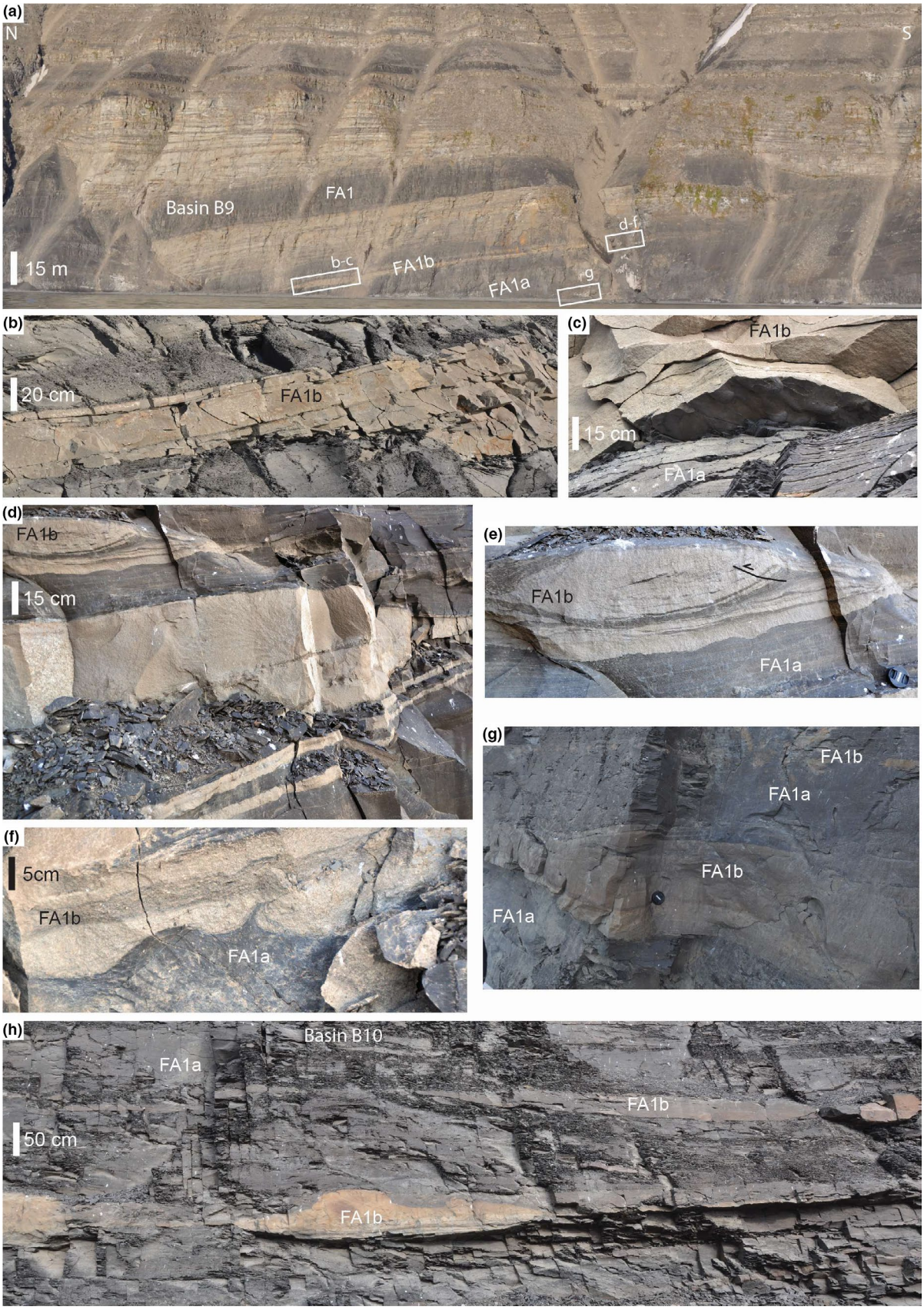

FIGURE 4 Examples of FA1. See text for the details

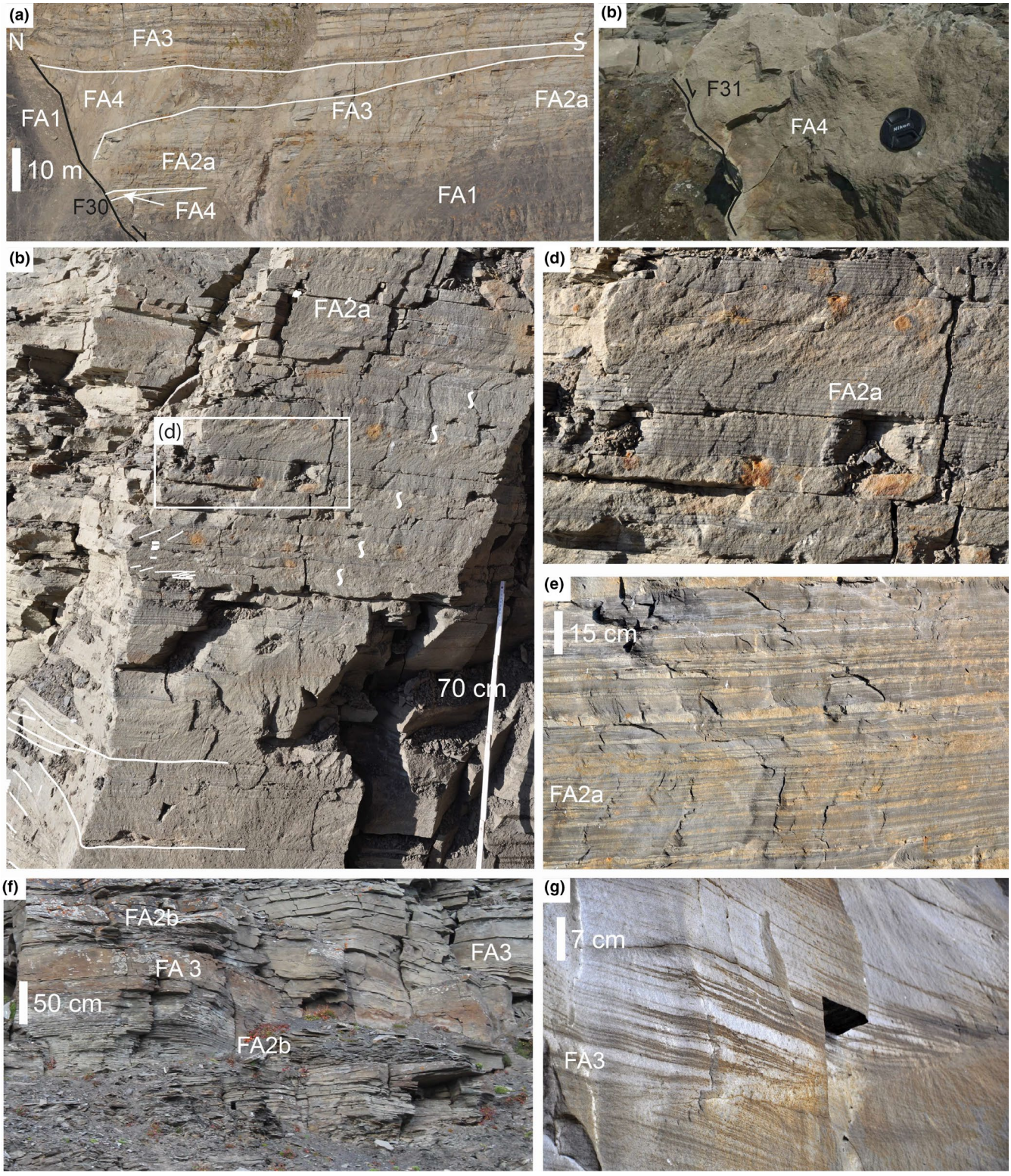

FIGURE 5 Examples of FA2, FA3 and FA4. See text for the details

from organic rich marine mudstones of the Botneheia Formation. Higher in the profile, FA1 occurs at the base of each CU and also in the lower part of the draping shale, where it has a sharp to erosive surface (Figure 4a).

FA1 is subdivided into two sub-facies associations FA1a and FA1b. FA1a (Figure 4) is composed of structureless to laminated mudstones with scattered marine shell fragments and rare to no bioturbation (Facies K). FA1b consists of

dm- to 1 m thick, very fine- to fine-grained structureless sandstone beds and lenses (Facies A, Table 1). The base of sandstone beds is sharp to erosive, with scouring and sole marks such as gutter casts, flutes and groove marks. Load structures, for example ball-and-pillow and cm-scale mud flames (Figure 4b,c) are common in the lower part of the sandstone beds, whereas faint plane-parallel lamination developed in their upper parts (Facies B). Soft-sediment deformations such as convolute lamination and mud clasts are locally abundant. Few individual FA1b's sandstone beds extend over a distance of more than 200 (Figure 4a). In addition to the sandstone beds, FA1b consists of intervals with mixed sandstones and mudstones, forming cm- to dm-thick lenses and dm- to m-thick ball-and-pillow structures with associated deformation structures, such as folds and cm-scale thrust faults (Figure 4e). FA1b also contains mudstone with planar to wavy structures and mm- to cm-thick siltstone and sandstone lamina (Facies J) as well as mm- to cm-thick and up to 10-cm-long sand lenses (Figure 4g). Rarely, very fine- to fine-grained, 1- to 2-dm-thick sandstone beds with wave ripples and hummocky cross-stratification are recognized (Facies F and G).

Interpretation

Thick mudstones with marine shell fragments assigned to FA1a represent a low-energy environment, with mud probably deposited from hypopycnal flows (e.g. Mulder, Syvitski, Migeon, Faugeres, & Savoye, 2003). The scarcity of wave-related structures and hummocky cross-stratification suggests that FA1a was deposited below the storm wave base. Structureless mudstone beds could represent completely burrowed mud. Thick sandstone beds with erosive lower boundaries and associated intense soft sediment deformation of FA1b suggest that these sediments were deposited as a resulted of hyperpycnal, high-density, gravity flows in a slope to basin floor setting (e.g. Mulder et al., 2003; Mutti, Tinterri, Benevelli, Biase, & Cavanna, 2003). Thin lamina and lenses of silt to very fine sandstone in the mudstone suggest deposition from distal density currents. Generally, FA1 is interpreted to represent prodelta to distal delta front deposits, in agreement with previous interpretations by Edwards (1976). Episodic deposition from density currents is represented by the sharp-based sandstone beds of FA1b intersecting the mud deposits of FA1a. The common occurrence of soft sedimentary structures suggests instability of the slope, such as gravitational collapse of the delta slope or very rapid sedimentation from a high river discharge during floods (Mutti et al., 2003). Alternatively, fault-controlled slope steepening due to fault block rotation or collapse of sediments triggered by seismic events (earthquakes) could also produce similar sedimentary structures (Nemec et al., 1988).

4.1.2 | FA2: tidal heteroliths

Description

FA2 consists of 2-dm to 3-m thick, lenticular and wavy-bedded heteroliths (Facies I and J; Table 1) alternating with light grey, fine-grained, 1- to 3-dm thick, low-angle cross-stratified sandstone beds that contain single and double mud drapes (Facies C). FA2 (Figure 5c,d) occurs either as 5- to 8-m thick, inclined heteroliths (FA2a) organized as coarsening-upward units, or as 2- to 6-m thick, tabular beds of heteroliths (FA2b) interbedded with cross-stratified sandstones of FA3 (Facies D). Occasional bioturbation is represented by scattered *Skolithos* burrows. Rhythmic alternations in thick and thin lamina inside the planar to wavy-bedded heterolithic succession occur locally (Facies I and J). Locally, dm-thick beds of sandstone with flaser bedding (Facies H), symmetrical ripples (Facies G) and/or plane-parallel lamination (Facies B) occur. The lower boundaries of the sandstone beds are either gradual or sharp, whereas their tops are commonly characterized by wave ripples. Localized intervals contain hummocky cross-stratification (Facies F). In lower parts of FA2, towards the gradual boundary with the underlying FA1, cm-scale soft-sediment deformation and loading structures are common. FA2 is capped by cross-stratified sandstones with mud drapes of FA3.

The 5- to 8-m thick, coarsening-upward heterolithic intervals of FA2a with inclined bedding consists of 3- to 5-m-high individual sets, that extend laterally over 50–75m. Their shape is tangential to planar, and they downlap on underlying layers. The occurrence of sandstone beds is accompanied by a thickness increase in the beds towards the north of the outcrop section. Heterolithis dominate towards the crest of the hanging wall fault blocks and the 'bottomset' position of the IHS. The dip angle of the IHS, when rotated back to the original depositional position by flattening on the top of CUs, ranges from 1 to 20 degrees. Foresets dip southwards, away from basin-bounding faults (Figure 5a). Therefore, the IHS appears to climb up the hanging wall dipslope in the half-grabens. Bidirectional currents towards the west and east are recorded in 2- to3-dm thick, low-angle cross-stratified sandstone beds, as for instance seen in the CU2 of basin B9 (Figures 6 and 7d-e). These bidirectional currents were transverse to the IHS dip direction.

Tabular intervals of FA2b can be traced laterally from north to south over 300 m. Typically, FA2b forms 5- to 6-m-thick coarsening-upwards intervals (basin B1), but occasionally fining-upward 1- to 2-m-thick beds are observed (e.g. CU1, Basin B1, Appendix S1).

Interpretation

FA2 shows numerous indicators of tidal influence and modulation, such as mud drapes, flaser bedding, sandstones

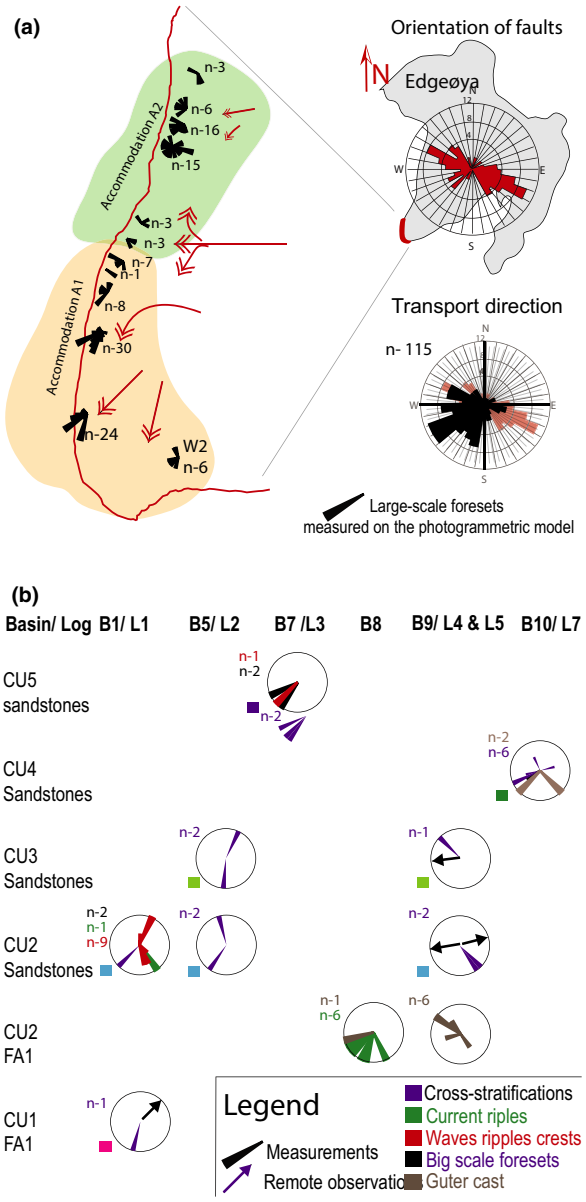

FIGURE 6 Orientation of transport indicators presented in rose diagrams, where *n* = number of measurements: (a) tens to hundreds of metres scale foresets within CU4 (green colour) and CU5 (orange colour) measured on the photogrammetric model; (b) compilation of field measurements of transport directions recorded within individual basins and CUs

with oppositely dipping foresets (`herringbone cross-stratification´), as well as the development of a variety of heteroliths, and cyclical bundling of various bedforms. The m-scale, heterolithic intervals of FA2a with inclined bedding are interpreted as 'inclined heterolithic stratification' sensu Thomas et al. (1987). Rhythmic alternations of thick and thin lamina are interpreted as tidal bundles (Figure 5c,d; e.g. Nio & Yang, 1991). The aforementioned structures suggest a distal deposition in a tidally affected, lower delta-front environment (e.g. Longhitano, Mellere, Steel, & Ainsworth, 2012; Willis, 2005). This interpretation is supported by the conformable position of FA2 above thick successions of deeper shelf deposits of FA1, and below the cross-stratified sandstones of FA3. Noticeably, a lack of mouth bars, erosive surfaces and typical channel geometries with infill facies suggest deposition at a distance from the delta top. Sand delivered to the basin has been further redistributed by tidal currents over the delta front and shallow shelf (e.g. Longhitano et al., 2012; Willis, 2005). The presence of sparse wave ripples, and sporadic HCS suggest periodical reworking of the sediment close to the storm wave base.

The development of FA2a and FA2b differs depending on the position and geometry within the fault-bounded basins. FA2a's combination of IHS associated with tidal current indicators and bi-modal transport direction transverse to the dip of the master bedding, suggests that the IHS master bedding represents lateral accretion surfaces developed within a tidal bar. Their development is likely the result of west-east oriented tidal currents. Lateral accretion surfaces are commonly ascribed to lateral migration of subaqueous tidal bars (López-Blanco, Marzo, & Muñoz, 2003; Olariu, Steel, Dalrymple, & Gingras, 2012; Olariu, Olariu, Steel, Dalrymple, & Martinius, 2012). FA2a is interpreted as a free-standing tidal bar or compound tidal bars detached from the delta front/top (e.g. Longhitano et al., 2012; López-Blanco et al., 2003; Olariu, Olariu, et al., 2012).

Tabular heteroliths of FA2b that alternate with cross-stratified sandstones of FA3 are interpreted as distal equivalents of forward migrating tidal compound dunes, described in the next section (e.g. Longhitano et al., 2012; Olariu, Steel, et al., 2012; Willis, 2005).

4.1.3 | FA3: tidal dunes

Description

FA3 consists of dm- and m-scale beds of fine to medium-grained, planar and trough cross-stratified sandstone with tangential foresets (Facies D; Table 1). FA3 also contains 1- to 3-dm thick, structureless sandstone beds (Facies A) and sandstone with flaser bedding (Facies H). Trace fossils are rare in FA3. Locally, in the lower part of FA3 units, 1- to 2-dm-thick current rippled sandstones (Facies E) occur. Single and double mud drapes are widespread. Locally, dunes with oppositely dipping foresets are observed (Figure 6b). Vertically stacked beds of FA3 deposits are arranged in 10- to 15-m thick, thickening and gently coarsening-upward sandstone intervals. The base of FA3 is either sharp, or represents gradual transition from deposits of FA2, or occasionally FA1. FA2a- FA3 couples form the upper parts of CUs. Alternatively, dm- to 1- to 2-m-thick beds of FA3 alternate with FA2b in metre-scale coarsening-upwards intervals (e.g.

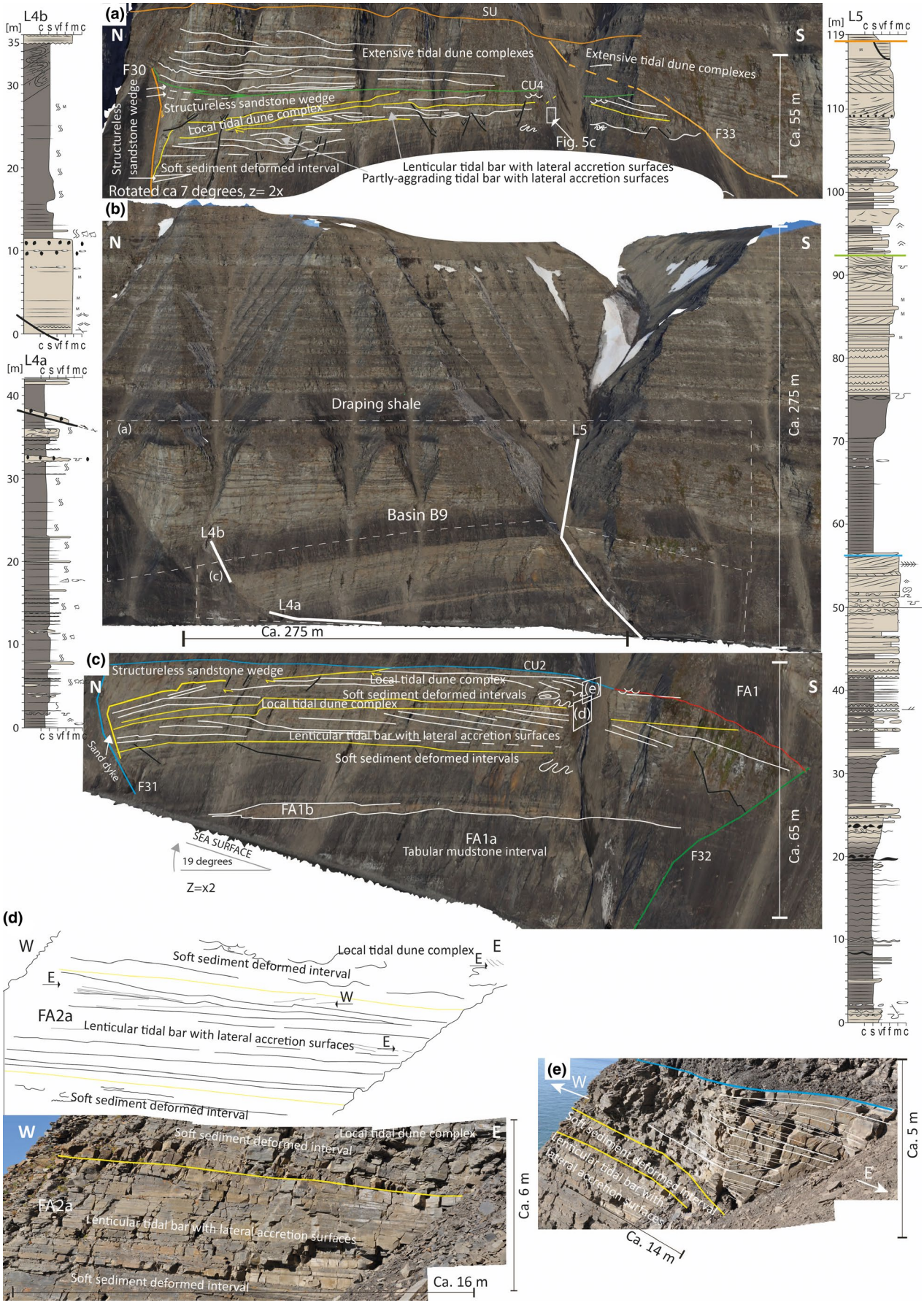
L4b
[m]
c s vf f m c
35
30
20
10
0
(a)
N
S
SU
Extensive tidal dune complexes
Extensive tidal dune complexes
F30
CU4
Structureless sandstone wedge
Structureless sandstone wedge
Local tidal dune complex
Fig. 5c
F33
Ca. 55 m
Soft sediment deformed interval
Lenticular tidal bar with lateral accretion surfaces
Partly-aggrading tidal bar with lateral accretion surfaces
Rotated ca 7 degrees, z= 2x
L5
[m]
119
110
100
90
80
70
60
50
40
30
20
10
0
(b)
N
S
Draping shale
Ca. 275 m
(a)
L5
Basin B9
L4b
(c)
L4a
Ca. 275 m
L4a
[m]
40
30
20
10
0
(c)
N
S
Structureless sandstone wedge
CU2
Local tidal dune complex
Soft sediment deformed intervals
Local tidal dune complex
(e)
(d)
FA1
Lenticular tidal bar with lateral accretion surfaces
Soft sediment deformed intervals
Sand dyke
F31
FA1b
SEA SURFACE
19 degrees
Z=x2
FA1a
Tabular mudstone interval
F32
Ca. 65 m
(d)
W
E
Local tidal dune complex
E
Soft sediment deformed interval
E
W
FA2a
Lenticular tidal bar with lateral accretion surfaces
E
Soft sediment deformed interval
W
Soft sediment deformed interval
Local tidal dune complex
E
FA2a
Lenticular tidal bar with lateral accretion surfaces
Soft sediment deformed interval
Ca. 16 m
Ca. 6 m
(e)
W
Soft sediment deformed interval
Lenticular tidal bar with lateral accretion surfaces
E
Ca. 14 m
Ca. 5 m

FIGURE 7 Basin B9 with marked faults, flooding surfaces and architectural elements. For the colour code of the flooding surfaces see Figure 3e. (a) Fragment of the photogrammetric model with CU3, vertically exaggerated by 2 and flattened by 7 degrees, interpreted in LIME; (b) fragments of the photogrammetric model of Basin B9 showing the position of logs L4 and L5 and outlines of figures (a) and (c); (c) Fragment of photogrammetric showing lower CU2: the model is interpreted in LIME, flattened by 19 degrees, vertically exaggerated by 2, with outlines of figures (d) and (e); (d) sketch and photograph of bidirectional transport directions within sandstone beds of lenticular tidal bars with lateral accretion surfaces in CU2. (e) A photograph of latteraly restricted tidal dune complex located in the uppermost part of CU2

Basin B1). Noticeably, transport directions in FA3 vary between stratigraphic levels.

Interpretation

FA3 is dominated by tangential cross-stratified amalgamated sandstones interpreted as deposits of straight crested and sinuous dunes, developed in response to unidirectional and bidirectional currents, likely associated with tidal circulation processes (Anderton, 1976). Abundant tidal indicators and tabular beds observed in cross sections along foresets dip direction suggest deposition of forward-migrating subaqueous tidal dunes, similar to sand waves in modern subtidal environments (e.g. Olariu, Steel, et al., 2012; Willis, 2005). The structureless texture found near the faults in some beds is interpreted as the result of rapid deposition under high-energy conditions (e.g. Mutti, 1992). Lack of trace fossils indicates unfavourable conditions for burrowing organisms, potentially due to rapid sand deposition or, alternatively, to transient brackish conditions (e.g. Nemec et al., 1988).

The high sand content and numerous tidal indicators might suggest deposition in a position more proximal and/or more tidally-influenced than FA2. However, sand waves are usually disconnected from the delta front/top sandstones, as they reflect redistribution by tidal currents across a shallow shelf (e.g. Longhitano et al., 2012; Willis, 2005). Similar to FA2, a general lack of typical delta front facies (mouth bars, distributary channels) supports this interpretation. Locally, in basin B1, alternation of FA3 with tabular tidal heteroliths of FA2b suggests interfingering of distal and proximal parts of dune fields, similar to forward-accreting tidal dune fields reported in the Ager Basin (Spain; Olariu, Steel, et al., 2012). There, they reflect tidally reworked sediments deposited in a confined, marine strait (Olariu, Steel, et al., 2012). Rossi et al. (2017) also reported similar tidal dune fields detached from a delta within the narrow, structurally controlled, tide-affected Calabria strait (Southern Italy).

4.1.4 | FA4: mass-flow sandstone deposits

Description

FA4 is characterized by structureless, fine- to medium-grained sandstone bodies (Facies A) with mud clasts (Figure 5a,b). The mud clasts occur within the structureless sandstone. FA4 forms distinct sandstone wedges that thicken towards the faults in the uppermost parts of the CUs in half-grabens. The bases of the wedges are either sharp and conformable, or gently undulating with truncation of underlying strata of FA2 and FA3 (Figure 5a e.g. CUs 2 and 3 in basin B9). The wedges range in heights of 13–17 m. At places, these wedges show stacked 1- to 5-m-thick sandstone beds that are separated by metre-wide, cm-thick mud layers. Each wedge has a flat top that corresponds to the upper boundary of CUs.

Interpretation

The metres-thick, structureless sandstone deposits with sharp to erosive base and flat tops are interpreted as high energy, subaqueous mass flow deposits (grain flows; Mutti, 1992). The fine- to medium-grained size is specific to FA 4 and could indicate discharge from a river mouth. However, the occurrence of angular mud-clasts suggests erosion and redistribution of sediments that originated near the site of deposition.

4.2 | Architectural elements

Based on the vertical and lateral distribution of facies associations and their geometries, the studied sedimentary succession can be grouped into eight distinct architectural elements (summarized in Figure 8). The stacking patterns of the various architectural elements allow a further interpretation of depositional settings beyond that of the facies associations.

4.2.1 | Tabular mudstone intervals

Tabular mudstone intervals consist of 15- to 25-m thick, symmetric successions of FA1 (Figure 8). Tabular mudstone intervals are 100- to 900-m-wide bodies that exhibit gradual upper boundaries with the deformed deposits of soft sediment deformed intervals (Figure 7). Alternatively, in the lower part of CU5, the tabular mudstone interval grades into forward migrating laterally extensive tidal dune complex that is exposed for over 4 km.

4.2.2 | Mudstone wedges

Mudstone wedges are asymmetric elements that consist of FA1. Mudstone wedges show maximum thickness of 15–25 m close to the bounding listric faults and widths of 100- to 450 m

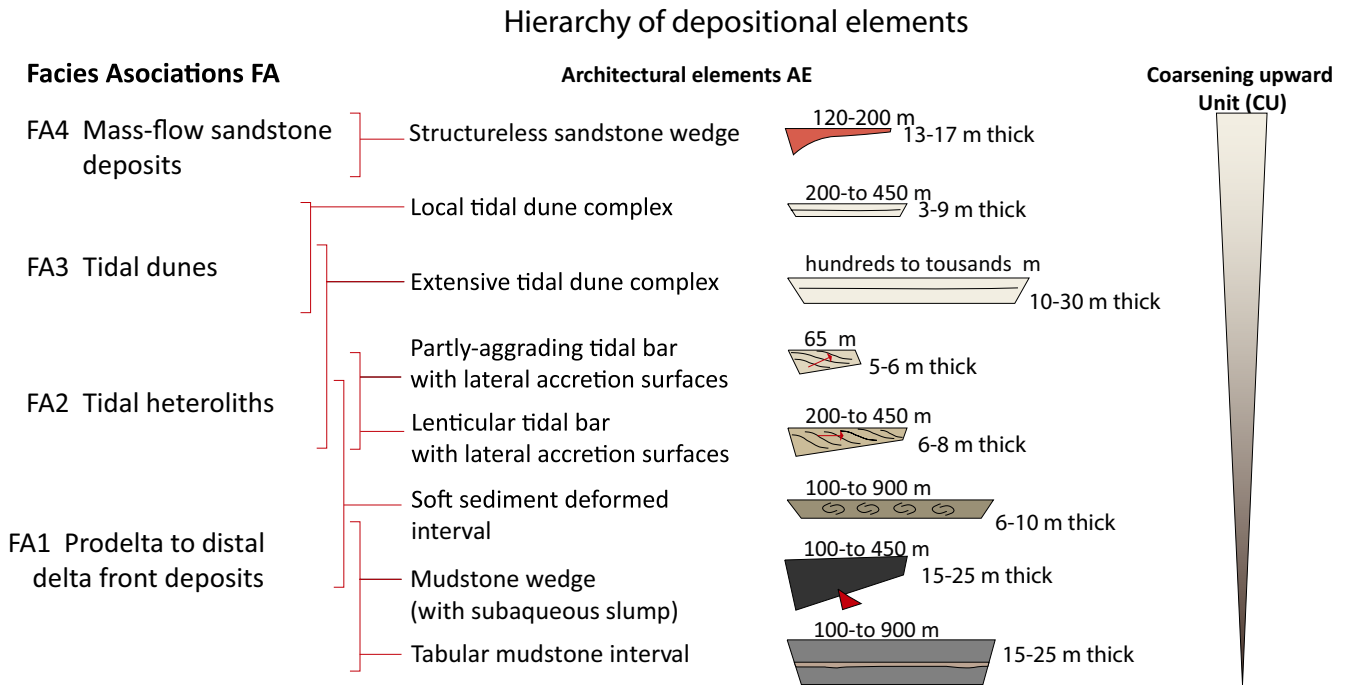

FIGURE 8 A conceptual model of architectural elements described in the text

(Figure 8). The occurrence of mudstone wedges is less common than tabular mudstone intervals. The mudstone wedges are well exposed in several locations, as part of CU4 in basins B1 and B6 (Figures 3 and 9e). Adjacent to master faults, mudstone wedges host triangular prisms of structureless, light grey to grey sediments, which are 6–10 m high and 35–50 m long (Figure 9e). These highly wedge-shaped deposits have not been logged due to the access limitation and are recognized only as a photographic-facies in pictures and in the photogrammetric model. The prisms can be linked with erosional surfaces on the adjacent footwall block (Figure 9c–e), suggesting they relate to subaqueous slumps from failure of exposed fault-scarps and footwall strata. Hence, truncation surfaces, presented in red in Figure 9e, mark the source of sediments removed from the footwall and redeposited as subaqueous mass flows. The triangular prisms are further draped by mudstones. Overall, the mudstone wedges thicknesses of 12–17 m measured on the photogrammetric model next to faults (Figure 9e) are considered to represent the maximum height of escarpments on the basin floor during periods with low sedimentation rates.

4.2.3 | Soft sediment deformed intervals

Soft sediment deformed intervals are present in all grabens and half-grabens. They consist of 4–10 m thick intervals of FA1 and FA2 with intense soft sediment deformation structures (Figure 10c–e). The degree of deformation ranges from cm-to-m scale growth faults and convoluted lamina, increasing to ball-and-pillow structures, m-scale folds and overturned bedding, before being eventually almost completely homogenized. The intensity and diverse style of disturbance within the soft sediment deformation occurred in overpressured, partly liquefied deposits transported as slumps over dm- to m-scale distances. Development of small growth faults, however, links the soft sediment deformed intervals with activity on the basin-bounding faults. Noticeably, the location of the intervals along half-graben dip-slopes suggests a relationship between soft-sediment deformation and fault-induced tilting of the basin floor due to the formation of roll-over anticlines.

4.2.4 | Lenticular tidal bars with lateral accretion surfaces

Lenticular tidal bars with lateral accretion surfaces are observed only in half-grabens (basins B4, B5, B8 and B9), where they are expressed as 6–8 m thick intervals of FA2a. Each single lenticular tidal bar is 3–5 m high, and extends laterally over 50-75m. The lateral accretion surfaces dip southwards, away from basin-bounding faults, indicative of a migration up the hanging wall dipslope (Figure 8). West- and eastward oriented bidirectional currents in low-angle cross-stratified sandstone beds (CU2 in the basin B9; Figure 6) suggest tidal currents nearly parallel to the half-graben axis. In conclusion, lenticular tidal bars with lateral accretion surfaces formed elongated bodies which were confined to fault-induced accommodation and aligned with the half-graben bounding fault.

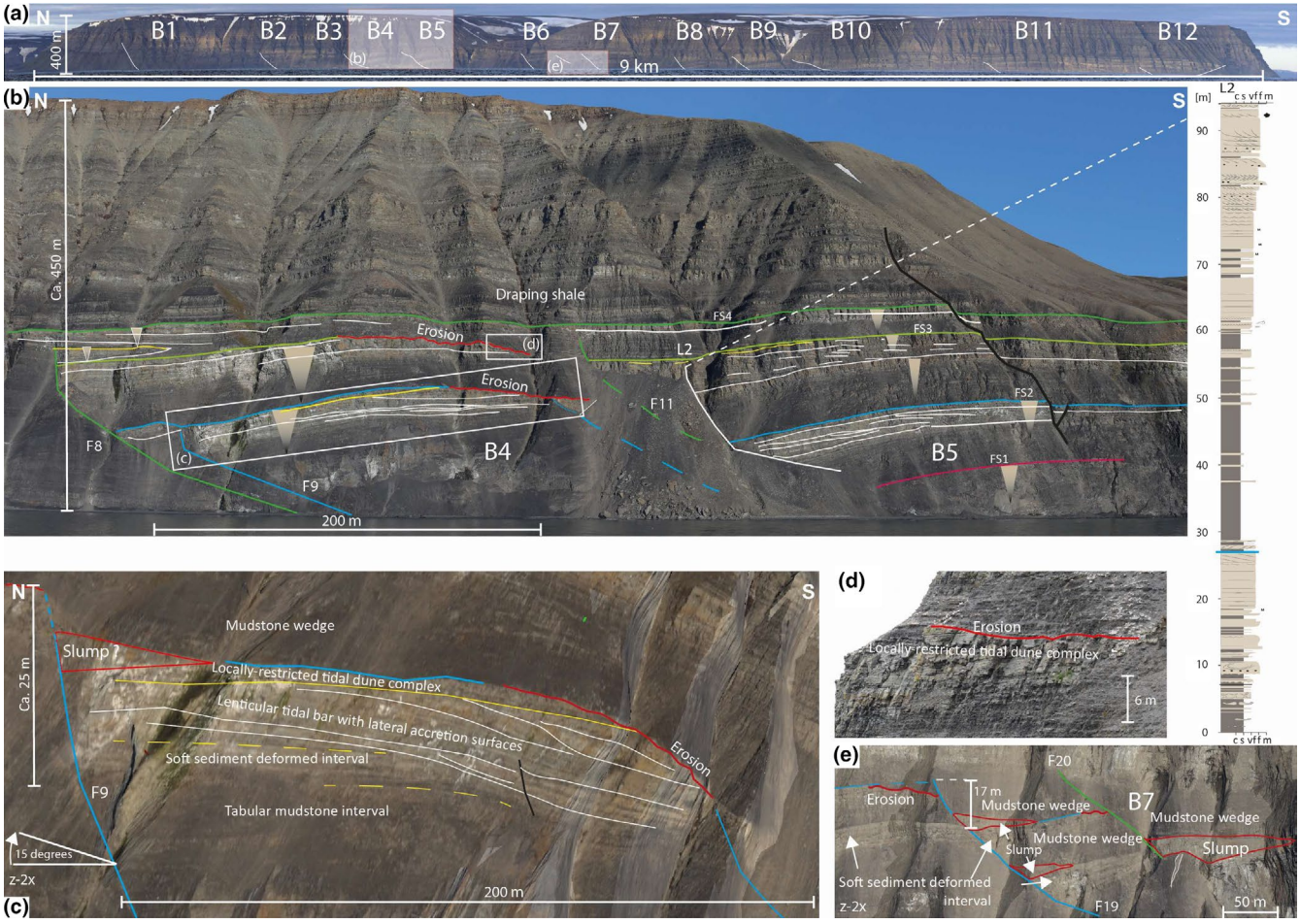

FIGURE 9 Photographs of growth basins B4 and B5 showing the distribution of architectural elements: notice the subaqueous slides and associated erosive surface marked in red. The photogrammetric model presented in figures (c) and (e) is interpreted in LIME. For the colour code of the flooding surfaces see the Figure 3e. See Appendix S7 for uninterpreted version

4.2.5 | Partly aggrading tidal bars with lateral accretion surfaces

Partly aggrading tidal bars with lateral accretion surfaces have been observed only in the CU3 in basin B9 (Figure 7a). This type of tidal bar is a variation of tidal bars with lateral accretion surfaces. It shows shorter and steeper, partly aggrading IHS that are 5 m high, with a 50 m lateral extent. Partly aggrading tidal bar formed in the half-graben adjacent to the fault.

4.2.6 | Laterally extensive tidal dune complexes

Laterally extensive tidal dune complexes usually form the upper component of CUs that are developed in grabens (basins B1 and B11) and are common in CUs 4 and 5. They consist of hundreds of metres wide, tabular and forward migrating sandstone dunes of FA3 and their distal equivalents, heteroliths of FA2b. Bidirectional palaeo-transport indicators within the dune complexes indicate a major tidal current direction towards the southwest, with a subordinate direction towards the northeast (Figure 6). In the graben B11, the laterally extensive tidal dune complex is characterized by a sharp contact with the underlying soft sediment deformed interval. This contact is interpreted as a tidal ravinement surface (TRS), outlined in Figure 10. In B11, the tidal dune complex consists of three tabular sand-sheets that are in total 10-m thick and continue over a distance of 850 m and extend laterally over 500 m B1.

4.2.7 | Laterally restricted tidal dune complexes

Laterally restricted, tidal dune complexes are expressed as tabular, 3- to 4-m thick elements extending up to 450 m and located in a topset position, above the lenticular tidal bars with lateral accretion surfaces. Laterally restricted tidal dune complexes are distinctly thinner and narrower than the laterally extensive tidal dune complexes (Figure

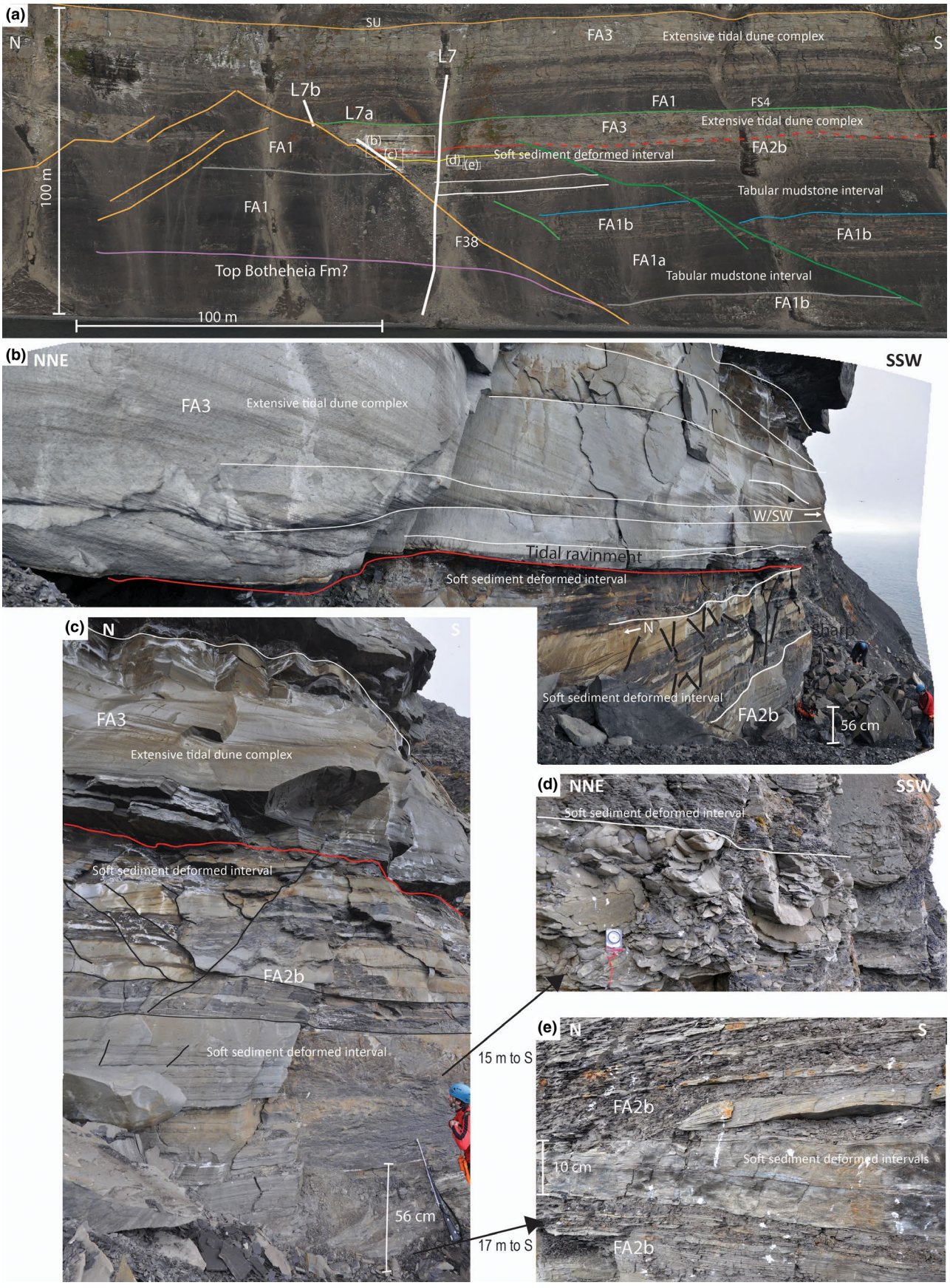

FIGURE 10 Graben B11 with marked architectural elements; notice tidal ravinement surface marked in red (b). For the colour code of the flooding surfaces see the Figure 3e. See Appendix S8 for uninterpreted version

8). Internally, laterally restricted tidal dune complexes are made up of sandstone-dominated, FA3, with beds showing m-scale foresets that dip westward (Figure 6b). Transport directions towards the west and southwest recorded by tangential cross-stratifications (e.g. CU3 in basin B9, Figures 6 and 10) conform to an interpretation of frontal migrating sinuous dunes, with currents sub-parallel to nearby faults. This mimic the sediment transport direction of the underlying tidal bars. As these migrating sinuous dunes overlay the tidal bars, these laterally restricted tidal dune complexes are interpreted as small fields of compound tidal dunes migrating over sand ridges. The transition from heteroliths-dominated tidal bars to sandy dunes reflects either an increase in tidal energy and/or sediment supply that could reflect a partly filled accommodation, as well as a change in sediment sourcing.

4.2.8 | Structureless sandstone wedges

Structureless sandstone wedges appear only in half-grabens adjacent to listric faults (e.g. top of CU3 in basin B9, Figure 7). The wedges are 13 to 17-m high and extend laterally over 120–200 m. The wedges consist of stacked sandstones of FA4. Locally, the wedges are associated with sand dikes injected downwards for 10–15 m along the bounding fault (e.g. CUs 2 and 3 in basin B9), as discussed in Maher et al. (2017) and Ogata et al. (2018). Distinct smaller structureless sandstone wedges that are dm- to 2-m thick and extending laterally over 45 m can be stacked on top of the larger sandstone wedge, as for instance demonstrated in the hanging wall of fault F30 (Figure 7a). These small wedges also appear in connection with the soft sediment deformation intervals. The asymmetrical geometry of sandstone wedges is related to syn-kinematic events. Smaller wedges may potentially represent a single increment of fault movement with throw of about dm- to 2-m scale, but the composite wedges likely reflect multiple fault-slip increments. Fault-created morphology, with associated accommodation, was filled with FA4's mass flow deposits. Some sand was likely sourced from the delta front and redistributed by mass flow along the hanging walls of the active faults. The flat tops of the wedges suggest (over-) fill of the fault-induced accommodation to the equilibrium profile followed by bypass of subsequent sediment. Alternatively, the uppermost parts of the wedges were eroded during subsequent transgressive episodes.

4.3 | Coarsening-upward units (CUs)

The first-order surfaces mapped on the photogrammetric outcrop model (Figure 3d,e) constitute the boundaries between CUs 1–5. Typically, the uppermost parts of CUs are represented by fine- to medium-grained sandstones interpreted as high-energy deposits of tidally reworked sandstone dunes (FA3) and/or mass flows sandstones (FA4). The sandstones have a sharp to locally erosive upper boundary towards the marine mudstones (FA1) that form the lowermost part of overlying CU. These boundaries are defined as a flooding surfaces (FS; Marine flooding surface in Van Wagoner et al., 1988; see FS1-FS4 in Figure 3d,e). Some flooding surfaces can be mapped with high accuracy over an area of 10×15 km.

The CUs 1–3 are developed within half-grabens (B1-B10) and grabens (B11 and B12) and are disconnected by horsts (Figure 3e). The thickest, up to 35-m thick, sandstone package was deposited in B1. Palaeo-transport direction recorded by density currents in FA1b (gutter cast within CU2 in B9; Figure 6b) was towards the northwest, near-parallel to the fault strike. Dunes and m-scale foresets record bi-modal transport direction towards the southwest and northeast. CU4 in the northern part of Kvalpynten is partially affected by faulting, whereas, in the south, it was deposited within wide, fault-bounded basins B10-B12. The palaeo-transport directions recorded within CU4 in the northern part show a divergent pattern with one component near-parallel to the growth faults (Figure 6a,b).

CU5, observed only in the southern part of the study area (Figure 3e), forms a coarsening-upward and coarsening-northward unit that is laterally extensive (over 5 km). Very-low angle, large-scale foresets (Figure 6a) recorded progradation towards the southwest. These foresets average 500 m in length and 10 m in height.

The top of the uppermost CU5 is capped by the mudstones of FA1's draping shale. At the base of the draping shale (log L5 in Figure 7), a c. 0.5-m thick, mottled, rust coloured sandstone horizon has been recognized and interpreted as a soil profile (Appendix S4 and S6l). This sandstone is interpreted as a sub-aerially exposed surface (SAES; Figure 3e) developed as a consequence of an abrupt shoreline progradation, prior to transgression and deposition of the mudstones above the entire fault array.

4.4 | Fault control on accommodation

Four types of accommodation recognized within CUs 1–5 are interpreted to represent the rate of faulting and fault geometry, as summarized in Figure 11a, and described below:

1. Symmetrical syn-kinematic accommodation developed in grabens bounded by oppositely dipping but kinematically connected planar faults with similar offset (e.g. basin B11). The accommodation was equally distributed across the graben, as evident by a tabular geometry of the sedimentary fill.
2. Asymmetrical syn-kinematic accommodation generated in half-grabens bounded by south-dipping, listric faults.

Fault geometry caused roll-over folding and enforces asymmetry in the basin, as well exposed in basins B2, B8 and B10 (Figure 3). The highest rates of accommodation creation occurred adjacent to faults and decreased up the dipslope, as reflected by an overall wedge shape of the syn-kinematic basin fill. In basins with ongoing faulting, hanging wall strata gradually rotated during progressive growth of roll-over anticlines.

3. Late-kinematic accommodation is illustrated by the deposits of CU4 (Figure 3), which form a continuous sandstone belt. This belt was perturbed by faulting which accrued c. 10-m offset. The thickness variations along the sandstone belt associated with the undulating base is due to enhanced sagging above pre-existing basins. Sagging caused renewed fault activity that triggered movement on upper fault segments, which resulted in development of small hanging wall growth wedges (Figures 9b and 11c).
4. Post-kinematic accommodation correlates with deposits of CU5, which were deposited as a belt that extends laterally over 5 km and are unaffected by syn-sedimentary faults (Figure 3). CU5 is, however, deformed by younger, post-sedimentary planar faults with dm- to 3-m-scale offsets.

For most of the half-grabens in the study area (B1, B4, B9; Figure 3) the oldest syn-kinematic strata have tabular shape. On the contrary, younger strata packages are wedge-shaped (see B4 in Figure 9cand B9 in Figure 7c). This upward and temporal change reflects initiation of basins as grabens first, bounded by planar faults, with faults moving simultaneously. Subsequently, activity became focused on the south-dipping faults, partly reactivating pre-existing structures, accompanied by the new development of listric faults. This change is fault style forced the basins to transition from grabens to half-grabens, as illustrated in Figure 11b.

4.5 | Influence of rates and distribution of accommodation on architectural elements stacking patterns

This study demonstrates that rates and distribution of accommodation creation directly controlled stacking of architectural elements within the five main coarsening upward units (Figure 11). The CUs 1–3 were deposited in fully compartmentalized basins, whereas sandstone-rich units are discontinuous across faults. Symmetrical versus asymmetrical lateral variations in the syn-kinematic accommodation impacted the shape of the entire basin fill as well as the development and stacking of the architectural elements. In grabens (Figure 11c), the CU starts with tabular mudstone intervals, and is overlain by the relatively thin soft sediment deformed intervals and the laterally extensive tidal dune complex. The dunes form horizontal, continuous sandstone sheets with approximately constant bed thickness in the basin. Lenticular tidal bars with lateral accretion surfaces and structureless sandstone wedges are missing in grabens.

Half-graben basins (Figure 11c) with asymmetrical accommodation are 200- to 400-m wide, with exception of the 850-m-wide basin B10. Typically, coarsening-upward sections consist of a basal mudstone wedge, overlain by soft sediment deformed interval and lenticular tidal bar(s) with lateral accretion surfaces. These lenticular tidal bars are overlain by laterally restricted tidal dune complex(es), which are eventually capped a by structureless sandstone wedge (Figure 11c). Some variations in stacking pattern occur, including the development of partly aggrading tidal bar with lateral accretion surfaces near the fault (e.g. CU4 in basins B9; Figure 7a). In some cases, couplets of underlying lenticular tidal bars with lateral accretion surfaces and laterally restricted tidal dune complexes are repeated, reflecting cyclic deposition that form lower-order coarsening-upward intervals within a CU unit (e.g. CU3 in basins B5; Figure 9b). 0.5- to 1-m-thick fining upward intervals can occur in the uppermost part of some CUs (CU3 in basin B9 and CU2 in B5), indicative of a waning of the energy, potentially associated with a localized increase in accommodation creation and/or system abandonment.

Late syn-kinematic accommodation is reflected in deposition of CU4. This unit varies in thickness from c. 10 m in the footwall blocks to c. 20 m in the basins. The hanging wall depocenters hosts fully developed CU4, with basal tabular mudstones and mudstone wedges overlain by south-westwards, forward-migrating laterally extensive tidal dune complex. Locally, 1- to 2-m-thick structureless sandstone wedges developed adjacent to faults. Contrastingly, in the footwall blocks, CU4 consist exclusively of laterally extensive tidal dune complex which exhibits a sharp, erosive lower boundary with the underlying CU (Figure 11c). This sharp lower boundary can be ascribed to erosion and sediment bypass in uplifted footwall position.

Post-kinematic accommodation is reflected by CU5 characteristics that consist of forward migrating laterally extensive tidal dune complex, which is overlain by tabular mudstone interval. In the southern part of the study area

FIGURE 11 (a) Schematic expression of four types of accommodation documented in Kvalpynten: grabens, half-grabens, late syn-kinematic accommodation and post-kinematic accommodation. (b) A conceptual evolution model of a half-graben evolving from an initial graben as the displacement along one fault starts to outpace the other (left) and a graben where both faults show similar displacement rates (right). (c) Stacking patterns of architectural elements defined in Figure 8, within different types of accommodation A1-A4

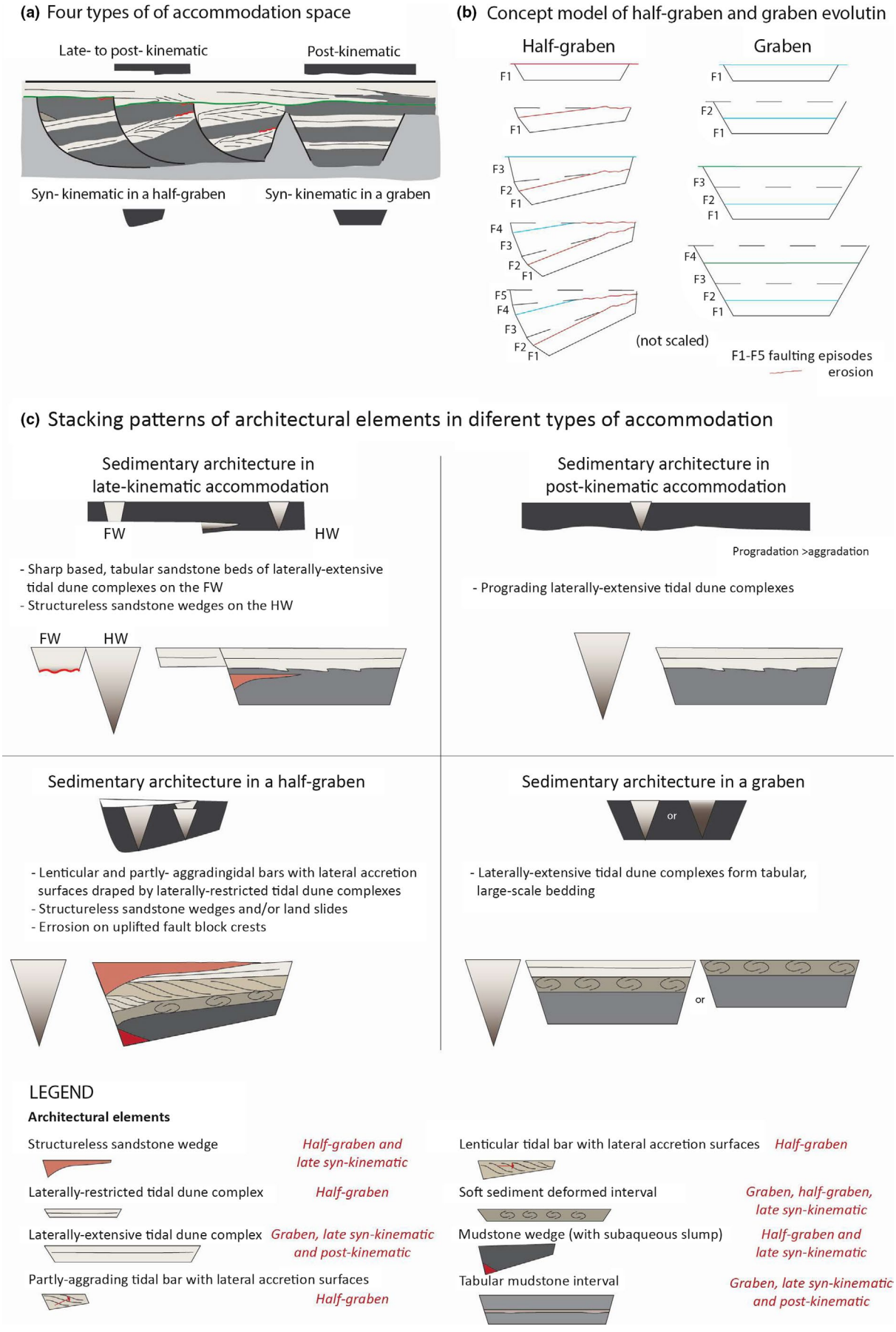
(a) Four types of of accommodation space
Late- to post- kinematic
Post-kinematic
Syn- kinematic in a half-graben
Syn- kinematic in a graben
(b) Concept model of half-graben and graben evolutin
Half-graben
Graben
F1
F2
F3
F4
F5
(not scaled)
F1-F5 faulting episodes
erosion
(c) Stacking patterns of architectural elements in diferent types of accommodation
Sedimentary architecture in late-kinematic accommodation
FW
HW
- Sharp based, tabular sandstone beds of laterally-extensive tidal dune complexes on the FW
- Structureless sandstone wedges on the HW
Sedimentary architecture in post-kinematic accommodation
Progradation >aggradation
- Prograding laterally-extensive tidal dune complexes
Sedimentary architecture in a half-graben
- Lenticular and partly- aggradingidal bars with lateral accretion surfaces draped by laterally-restricted tidal dune complexes
- Structureless sandstone wedges and/or land slides
- Errosion on uplifted fault block crests
Sedimentary architecture in a graben
or
- Laterally-extensive tidal dune complexes form tabular, large-scale bedding
LEGEND
Architectural elements
Structureless sandstone wedge
Half-graben and late syn-kinematic
Laterally-restricted tidal dune complex
Half-graben
Laterally-extensive tidal dune complex
Graben, late syn-kinematic and post-kinematic
Partly-aggrading tidal bar with lateral accretion surfaces
Half-graben
Lenticular tidal bar with lateral accretion surfaces
Half-graben
Soft sediment deformed interval
Graben, half-graben, late syn-kinematic
Mudstone wedge (with subaqueous slump)
Half-graben and late syn-kinematic
Tabular mudstone interval
Graben, late syn-kinematic and post-kinematic

(Figure 11b) CU5 is expressed as a coarsening-northward system with progradation towards the southwest (Figure 7a), as highlighted by very-low angle, large-scale foresets (500-m lateral extent, height of 10 m). This suggests that post-kinematic regional accommodation increased southwards and was filled with sand sourced from the east or northeast, accompanied by the development of (sub)tidal sandwaves migrating south-westward.

5 | DISCUSSION

5.1 | Sedimentary response to faulting events in distinct sea level sediment supply scenarios

Single-faulting events and intervening periods of quiescence are interpreted to have had a significant effect on the stacking pattern of architectural elements within CUs. This impact can be examined for different settings of relative sea level and sediment supply, as illustrated in three scenarios in Figure 12a–c. The deposition that occurred during or shortly after faulting was associated with rapid redistribution of sediments, which were likely sourced from areas proximal to the bounding faults in the footwall. Post-kinematic deposition expresses passive fill of available accommodation. (a) In a high relative sea-level/low sediment supply setting (Figure 12a), the syn-kinematic deposition led to the deposition of intervals hosting FA1b's high-energy deposits of density currents interfingering with tabular mudstone intervals and subaqueous slumps within mudstone wedges. These sandstone-rich deposits subsequently were draped by post-kinematic mudstones. (b) In an intermediate sealevel/sediment supply setting (Figure 12b), the loose sediments in the hanging wall blocks were intensely affected by soft sediment deformations. Soft sediment deformation was likely a result of basin floor tilting and shaking during slip events on listric faults. Additionally, small structureless sandstone wedges developed in half grabens (Figure 7a). Lenticular tidal bars with lateral accretion surfaces or distal laterally extensive tidal dune complexes passively filled the post-kinematic accommodation space. The position of partly aggrading tidal bars with lateral accretion surfaces adjacent to the fault likely reflects the post-kinematic deposition in a higher and more localized accommodation than tidal bars with lateral accretion surfaces. (c) In a low relative sea-level/high sediment supply setting (Figure 12c), the syn-kinematic deposition in half-grabens led to the deposition of structureless sandstone wedges filling available accommodation. Contrastingly, in graben, syn-kinematic deposits are not obvious and, where they occur, may be linked to the development of soft sediment deformation intervals. Laterally extensive tidal dune complexes passively filled the remaining post-kinematic accommodation.

5.2 | Impact of basin floor morphology on palaeo-tidal circulation

This study discerns distinct sedimentary architectures within tidally influenced, fault-bounded grabens and half-grabens in the distal part of a prograding deltaic system. The overall sediment palaeo-current pattern suggests a southwest dominating transport direction with subordinate northwest-southeast oriented flows (Figure 6). Laterally extensive tidal dune complexes found in the post-kinematic succession (CU5) and in wide graben fills (e.g. B10), recorded sediment progradation towards the southwest (Figure 6). These broad systems may reflect regional basin circulation (Figure 12b). This transport direction is modified in late-kinematic successions by faulting as determined by scattered palaeo-transport indicators (CU4; Figure 6a). The strongest fault-control on transport direction is expressed in narrow half-grabens (e.g. B9), where lenticular tidal bars with lateral accretion surfaces and laterally restricted tidal dune complexes developed axially to slightly obliquely to the bounding faults. Palaeotidal currents circulated northwest-wards to westwards, perpendicular to the southwest subregional direction recorded in CU5 (Figure 6).

Narrow half-grabens have a funnel-shaped topography, in which tidal currents were probably amplified, especially during ebb-tides. Hydraulic conditions of tidal currents in a narrow confinement may drive development of lateral migrating surfaces, resembling bank-attached point bars (Longhitano et al., 2012). Noticeably, the half-graben dipslopes of Kvalpynten consistently dip to the north (Figure 3) and sandstone beds within lenticular tidal bars gently thicken towards the north. Contrastingly, lateral accretion built southward (away from the bounding faults), up the dipslope towards shallower water. This highlights that fault-generated basin floor morphology played a major role in half-graben hydrodynamics, mainly by amplifying basin axis-parallel tidal currents in deeper parts. This funnelling effect waned towards shallower waters higher on

FIGURE 12 (a–c) Conceptual model of the development of pre-, syn- and post-kinematic architectural elements that depend on the rate of relative sea level/sediment supply. (d) Conceptual model of growth basins and their development in prodelta/lower front of a tidally-influenced delta with heteroliths and sand redistributed by tidal bars and dunes, detached from the delta front/delta top; inspired by López-Blanco et al. (2003); blue arrows mark tidal current orientations, red arrows mark the lateral accretion of tidal bars in a half-graben, whereas a green arrow mark forward accretion of tidal dunes in a graben

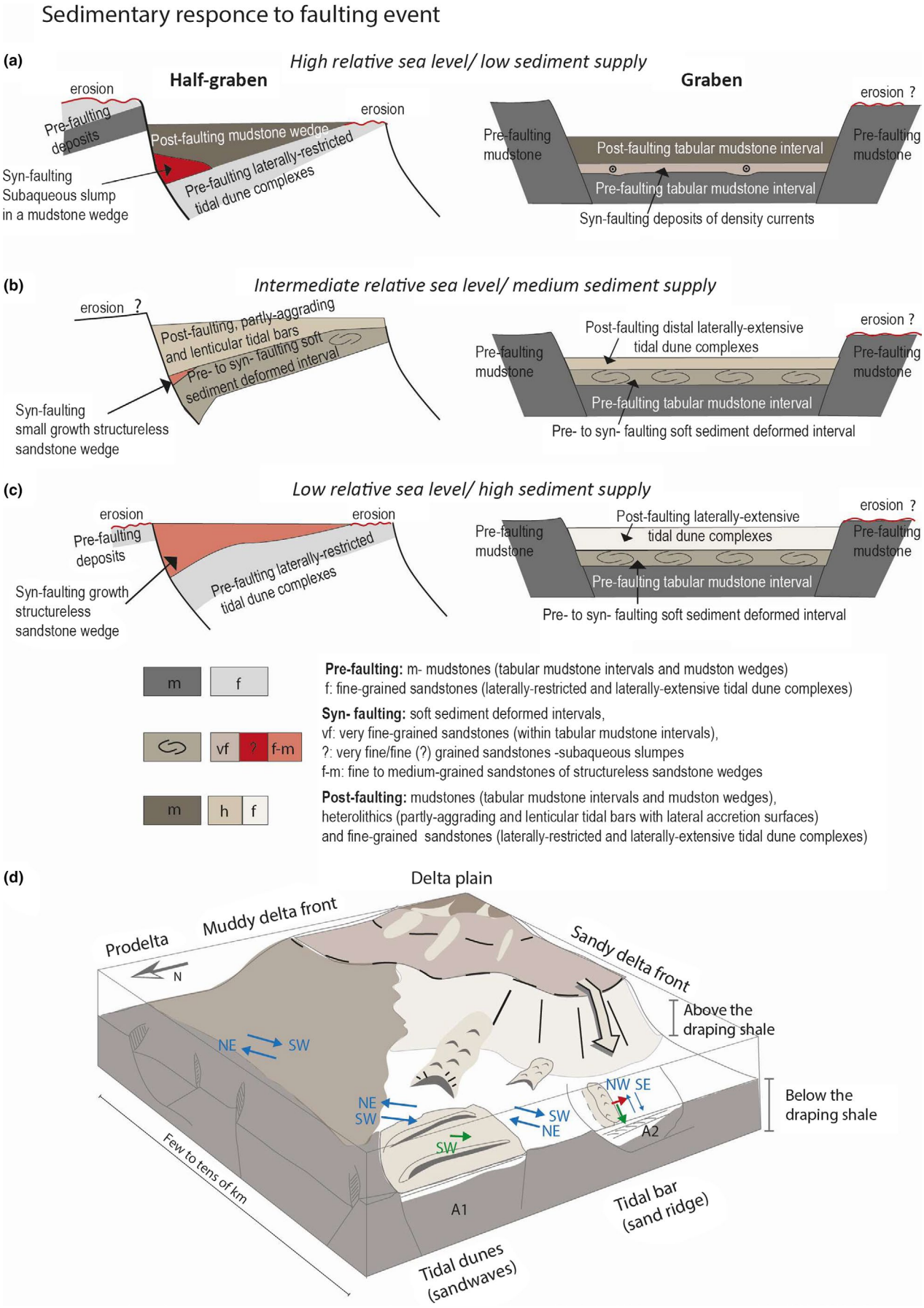
Sedimentary responce to faulting event
(a)
High relative sea level/ low sediment supply
Half-graben
erosion
Pre-faulting deposits
Post-faulting mudstone wedge
erosion
Pre-faulting laterally-restricted tidal dune complexes
Syn-faulting Subaqueous slump in a mudstone wedge
Graben
erosion ?
Pre-faulting mudstone
Post-faulting tabular mudstone interval
Pre-faulting mudstone
Pre-faulting tabular mudstone interval
Syn-faulting deposits of density currents
(b)
Intermediate relative sea level/ medium sediment supply
erosion ?
Post-faulting, partly-aggrading and lenticular tidal bars
Pre- to syn- faulting soft sediment deformed interval
Syn-faulting small growth structureless sandstone wedge
Post-faulting distal laterally-extensive tidal dune complexes
erosion ?
Pre-faulting mudstone
Pre-faulting mudstone
Pre-faulting tabular mudstone interval
Pre- to syn- faulting soft sediment deformed interval
(c)
Low relative sea level/ high sediment supply
erosion
Pre-faulting deposits
erosion
Pre-faulting laterally-restricted tidal dune complexes
Syn-faulting growth structureless sandstone wedge
Post-faulting laterally-extensive tidal dune complexes
erosion ?
Pre-faulting mudstone
Pre-faulting mudstone
Pre-faulting tabular mudstone interval
Pre- to syn- faulting soft sediment deformed interval
m
f
vf
?
f-m
m
h
f
Pre-faulting: m- mudstones (tabular mudstone intervals and mudston wedges)
f: fine-grained sandstones (laterally-restricted and laterally-extensive tidal dune complexes)
Syn- faulting: soft sediment deformed intervals,
vf: very fine-grained sandstones (within tabular mudstone intervals),
?: very fine/fine (?) grained sandstones -subaqueous slumpes
f-m: fine to medium-grained sandstones of structureless sandstone wedges
Post-faulting: mudstones (tabular mudstone intervals and mudston wedges),
heterolithics (partly-aggrading and lenticular tidal bars with lateral accretion surfaces)
and fine-grained sandstones (laterally-restricted and laterally-extensive tidal dune complexes)
(d)
Delta plain
Prodelta
Muddy delta front
Sandy delta front
N
NE
SW
Above the draping shale
NE
SW
SW
NW SE
SW
NE
A2
Below the draping shale
Few to tens of km
A1
Tidal bar (sand ridge)
Tidal dunes (sandwaves)

the dipslope, as accommodation was filled and the relief was healed.

5.3 | Internal versus external controls on development of CU units

Cycles of CU1-5 capped by flooding surfaces bear evidence of the syn and late/post-kinematic filling of the Kvalpynten basins. CUs 1–5 are 25- to 60-m thick on average, which is 2–4 times thicker than fault-induced accommodation; therefore, CUs cannot be entirely controlled by faulting. This is also supported by deposition of CU5, that is after fault activity. The individual positions of flooding surfaces in the hanging walls of growth faults constrain the interpretation of processes that controlled their development. Besides eustatic sea level variations, different rates of delta front progradation, autogenic delta lobe switching, differential compaction and fault- or sediment-loading-induced subsidence offer complementary controls on development of CU units and flooding surfaces.

Within half-grabens, fault-introduced basin floor topography during deposition of subaqueous slumps indicates a maximum relief of 12 to 17 m (mudstone wedges in Figure 9e). This value can be considered a proxy for a fault-induced accommodation increase for one/several faulting episode(s) during times of high relative sea level/low sediment supply (Figure 12a). Similarly, during low accommodation relative to sediment supply (Figure 12c) the 13–17 m thick structureless sandstone wedges can serve as a proxy for syn-kinematic accommodation increase. This also documents that faulting occurred in both, low and high rates of sediment supply.

Edwards (1976) interpreted the southerly dipping faults in Kvalpynten to form due to loading and gravitational collapse of delta front sandstones prograding from the north. Edwards' (1976) model contradict the recent, more regional understanding of the Upper Triassic deltaic deposits prograding towards north, north-west across the Barents shelf (Figure 1b; Anell et al., 2014, 2016; Glørstad-Clark et al., 2010, 2011; Høy & Lundschien, 2011; Klausen et al., 2015; Lundschien et al., 2014; Riis et al., 2008; Worsley, 2008). This study shows that growth faulting occurred in the prodelta position and corresponds to both, low and high rates of sediment supply. The growth fault system was dominated by listric faults that dip to the south and southwest, in a near-landward direction and against the prograding delta. The deepening of CU5 to the south and south-facing listric growth faults fit the model of a compaction-front arriving from a southerly direction, as advocated by Braathen, Midtkandal, et al. (Braathen, Midtkandal, et al., 2018) and Ogata et al. (2018). In this scenario, the deltaic system was prograding against and atop the roughly NE-SW oriented, palaeo-bathymetry (i.e. Svalbard platform). Ogata et al. (2018) discuss the regional differential compaction and instability along a gently inclined, long-lived delta-facing slope as trigger mechanisms for the growth faulting. In addition, deep-rooted tectonic faults of Carboniferous age were likely reactivated by far-field tectonics related to the late Triassic Uralide orogeny to the east (Anell et al., 2013; Ogata et al., 2018).

The palaeo-bathymetry in the NW Barents Shelf caused a significant decrease in the overall available accommodation for deltaic sediments prograding against the Svalbard Platform that impacted a lack of aggradation and differential advancement rates of the clinoforms (Anell et al., 2013, 2016). In Kvalpynten, the palaeo-slope and corresponding subsidence increase towards the south can explain the southwards deepening of CU5 deposits.

Growth faults impacted palaeo-bathymetric relief of the top of the Botneheia Formation during the deposition of the Tschermakfjellet Formation (Ogata et al., 2018). The stacking patterns of CU1-4 are unique to each basin, do not show any clear progradational or retrogradational trends and therefore may be considered as aggradational. In contrast to the regional decrease in subsidence (Anell et al., 2013, 2016), the local depocentres located in the hanging walls of the growth faults allowed for the aggradation of the CU1-4 deposits.

Tidal reworking of sediments can redistribute sand across the shelf, and lead to the development of tidal bars and dunes, that are detached from the delta front/top (Longhitano et al., 2012; Olariu, Steel, et al., 2012; Olariu, Olariu, et al., 2012; Rossi et al., 2016, 2017; Rossi & Steel, 2016; Willis, 2005). In Kvalpynten, tidal bars and dunes that migrated over a distance of few to tens of km and were detached from the tidally influenced delta front/top (Figure 12d), as similarly observed in the Roda Formation (Esdolomada Member) of the Tremp-Graus Basin in Spain, where tidal (shelf) bars are detached from the delta mouth by a distance of approximately 4 km (Olariu, Olariu, et al., 2012). In Kvalpynten, the distance between the tidal bars and dunes and the delta front/top is uncertain. The position of delta top for CUs 1–4 remains unknown. 4–5 km to the east of Kvalpynten (at Vogelberget; Figure 2) in the stratigraphic level corresponding to the CU5, Röhnert (2016) interpreted a succession of heterogeneous sandstone complexes as mixed energy (tidal and wave modified) channels and mouth bars with transport directions towards southwest. This succession and could represent the position of the delta front during the deposition of the uppermost CU5.

6 | CONCLUSIONS

This study documents the impact of growth faulting on the deposition of coarsening-upward units in the 400-m-high and 9-km-long cliffs of Kvalpynten, SW Edgeøya, Svalbard. The transition from prodelta mudstones to heterolithic tidal bars

and tidally reworked sandy dunes is interpreted to represent a distal part of the Upper Triassic seismic–scale deltaic system, which prograded north-westwards over the Barents Shelf. It is concluded that:

1. The stratigraphic succession fill is segmented by listric and planar growth faults into 12 isolated grabens and half-grabens situated in prodelta to delta slope.
2. The basin floor morphology was impacted by fault-scarps and progressive tilting of fault blocks that enhanced subaqueous erosion along the uplifted footwalls, triggered gravity-driven processes and introduced locally derived sediment into the grabens and half-grabens.
3. Narrow and elongated troughs in hanging walls amplified tidal energy that impacted the modality of sediment deposition.
4. Accommodation was controlled by growth faulting: fully compartmentalized syn-kinematic deposition occurred in grabens and half-grabens. In these basins, the dynamic nature of progressive fault-driven accommodation had a strong impact on the stacking patterns of sedimentary units. Architectural elements that relate directly to the rate of fault-induced accommodation were systematically stacked within the coarsening upwards units.
5. Late-kinematic deposition is expressed by continuous units, mildly influenced by compaction-driven faulting.
6. Post-kinematic accommodation has formed in response to regional subsidence and was filled by a south-westwards prograding system of mudstone passing into tidal dunes.

ACKNOWLEDGMENTS

The authors would like to acknowledge The University Centre in Svalbard for funding Smyrak-Sikora's research. Field work was supported by the Trias North Project (grant 234152/E30) financed by the Research Council of Norway and industry partners, Edison Norway, Lundin Norway, RWE Dea Norge, Statoil and Tullow Oil. We acknowledge Simon Buckley and the Virtual Outcrop Geology Group (Uni Research CIPR) for providing academic licenses for LIME. Berit Husteli and Luka Blažić are acknowledged for their contribution to the logs. Snorre Olaussen, Ivar Midtkandal and Harmon Maher are thanked for their comments and discussion on the research. The associate editor in Basin Research Cari Johnson and the reviewers Stefan Back, Luigi Bruno, and anonymous reviewer are acknowledged for their constructive comments to the manuscript.

DATA AVAILABILITY STATEMENT

The data that support the findings of this study are provided in the supplementary material.

ORCID

Aleksandra Smyrak-Sikora https://orcid.org/0000-0001-9321-1269
Alvar Braathen https://orcid.org/0000-0002-0869-249X
Kei Ogata https://orcid.org/0000-0002-4978-2854

REFERENCES

Ahlborn, M., & Stemmerik, L. (2015). Depositional evolution of the Upper Carboniferous – Lower Permian Wordiekammen carbonate platform, Nordfjorden High, central Svalbard, Arctic Norway. *Norwegian Journal of Geology*, *95*, 91–126.

Allen, J. R. L. (1982). *Sedimentary structures, their character and physical basis* (Vol. *1*). New York: Elsevier.

Anderton, R. (1976). Tidal-shelf sedimentation: An example from the Scottish Dalradian. *Sedimentology*, *23*(4), 429–458. https://doi.org/10.1111/j.1365-3091.1976.tb00062.x

Anell, I. M., Braathen, A., & Olaussen, S. (2014). The Triassic-Early Jurassic of the northern Barents Shelf: A regional understanding of the Longyearbyen CO_2 reservoir. *Norsk Geologisk Tidsskrift*, *94*, 83–98.

Anell, I., Braathen, A., Olaussen, S., & Osmundsen, P. T. (2013). Evidence of faulting contradicts a quiescent northern Barents Shelf during the Triassic. *First Break*, *31*(6), 67–76. https://doi.org/10.3997/1365-2397.2013017

Anell, I. M., Faleide, J. I., & Braathen, A. (2016). Regional tectono-sedimentary development of the highs and basins of the northwestern Barents Shelf. *Norsk Geologisk Tidsskrift*, *96*(1), 27–41. https://doi.org/10.17850/njg96-1-04

Ashley, G. M. (1990). Classification of large-scale subaqueous bedforms: A new look at an old problem-SEPM bedforms and bedding structures. *Journal of Sedimentary Research*, *60*(1), 160–172. https://doi.org/10.2110/jsr.60.160

Ashley, G. M., Southard, J. B., & BooTHRoyD, J. C. (1982). Deposition of climbing-ripple beds: A flume simulation. *Sedimentology*, *29*(1), 67–79. https://doi.org/10.1111/j.1365-3091.1982.tb01709.x

Baas, J. H., Best, J. L., & Peakall, J. (2016). Predicting bedforms and primary current stratification in cohesive mixtures of mud and sand. *Journal of the Geological Society*, *173*(1), 12–45. https://doi.org/10.1144/jgs2015-024

Back, S., & Morley, C. K. (2016). Growth faults above shale–Seismic-scale outcrop analogues from the Makran foreland, SW Pakistan. *Marine and Petroleum Geology*, *70*, 144–162. https://doi.org/10.1016/j.marpetgeo.2015.11.008

Back, S., Strozyk, F., Kukla, P. A., & Lambiase, J. J. (2008). Three-dimensional restoration of original sedimentary geometries in deformed basin fill, onshore Brunei Darussalam, NW Borneo. *Basin Research*, *20*(1), 99–117. https://doi.org/10.1111/j.1365-2117.2007.00343.x

Basilici, G. (1997). Sedimentary facies in an extensional and deep-lacustrine depositional system: The Pliocene Tiberino Basin, Central Italy. *Sedimentary Geology*, *109*(1–2), 73–94. https://doi.org/10.1016/S0037-0738(96)00056-5

Bergh, S. G., Maher, H. D., & Braathen, A. (2000). Tertiary divergent thrust directions from partitioned transpression, Brøggerhalvøya, Spitsbergen. *Norsk Geologisk Tidsskrift*, *80*(2), 63–81.

Bhattacharya, J. P., & Davies, R. K. (2001). Growth faults at the prodelta to delta-front transition, Cretaceous Ferron sandstone, Utah. *Marine*

and Petroleum Geology, *18*(5), 525–534. https://doi.org/10.1016/S0264-8172(01)00015-0

Bouroullec, R., Cartwright, J. A., Johnson, H. D., Lansigu, C., Quémener, J. M., & Savanier, D. (2004). Syndepositional faulting in the Grès d'Annot Formation, SE France: High-resolution kinematic analysis and stratigraphic response to growth faulting. *Geological Society, London, Special Publications*, *221*(1), 241–265. https://doi.org/10.1144/GSL.SP.2004.221.01.13

Braathen, A., Bælum, K., Maher, H. Jr, & Buckley, S. J. (2011). Growth of extensional faults and folds during deposition of an evaporite-dominated half-graben basin; the Carboniferous Billefjorden Trough, Svalbard. *Norwegian Journal of Geology/Norsk Geologisk Forening*, *91*(3), 131–161.

Braathen, A., Bergh, S. G., & Maher, H. D. Jr (1999). Application of a critical wedge taper model to the Tertiary transpressional fold-thrust belt on Spitsbergen. *Geological Society of America Bulletin*, *111*, 1468–1485.

Braathen, A., Midtkandal, I., Mulrooney, M. J., Appleyard, T. R., Haile, B. G., & van Yperen, A. E. (2018). Growth-faults from delta collapse–structural and sedimentological investigation of the Last Chance delta, Ferron Sandstone, Utah. *Basin Research*, *30*(4), 688–707. https://doi.org/10.1111/bre.12271

Braathen, A., Osmundsen, P. T., Maher, H., & Ganerød, M. (2018). The Keisarhjelmen detachment records Silurian-Devonian extensional collapse in Northern Svalbard. *Terra Nova*, *30*(1), 34–39. https://doi.org/10.1111/ter.12305

Bruce, C. H. (1973). Pressured shale and related sediment deformation: Mechanism for development of regional contemporaneous faults. *AAPG Bulletin*, *57*(5), 878–886.

Buckley, S. J., Ringdal, K., Naumann, N., Dolva, B., Kurz, T. H., Howell, J. A., & Dewez, T. J. (2019). LIME: Software for 3-D visualization, interpretation, and communication of virtual geoscience models. *Geosphere*, *15*(1), 222–235. https://doi.org/10.1130/GES02002.1

Burhannudinnur, M., & Morley, C. K. (1997). Anatomy of growth fault zones in poorly lithified sandstones and shales: Implications for reservoir studies and seismic interpretation: Part 1, outcrop study. *Petroleum Geoscience*, *3*(3), 211–224. https://doi.org/10.1144/petgeo.3.3.211

Caillet, G., & Batiot, S. (2003). 2D modelling of hydrocarbon migration along and across growth faults: An example from Nigeria. *Petroleum Geoscience*, *9*(2), 113–124. https://doi.org/10.1144/1354-079302-499

Cartwright, J. A., Mansfield, C., & Trudgill, B. (1996). The growth of normal faults by segment linkage. *Geological Society, London, Special Publications*, *99*(1), 163–177. https://doi.org/10.1144/GSL.SP.1996.099.01.13

Carver, R. E. (1968). Differential compaction as a cause of regional contemporaneous faults. *AAPG Bulletin*, *52*(3), 414–419.

Chandler, J. H., & Buckley, S. (2016). Structure from motion (SFM) photogrammetry vs terrestrial laser scanning. In M. B. Carpenter & C. M. Keane (Eds.), *Geoscience Handbook 2016, AGI Data Sheets* (5th edn.). Section 20.1. Alexandria, USA: American Geosciences Institute.

Cheel, R. J., & Leckie, D. A. (1993). Hummocky cross-stratification. *Sedimentology Review*, *1*, 103–122.

Cheel, R. J., & Middleton, G. V. (1986). Horizontal laminae formed under upper flow regime plane bed conditions. *The Journal of Geology*, *94*(4), 489–504. https://doi.org/10.1086/629053

Dallmann, W. K., Elvevold, S., Majka, J., & Piepjohn, K. (2015). Tectonics and tectonothermal events. In: Geoscience Atlas of Svalbard (Ed. by Dallmann, W.K.). *Norsk Polarinstitutt Rapportserie*, *148*, 175–223.

Dimakis, P., Braathen, B. I., Faleide, J. I., Elverhøi, A., & Gudlaugsson, S. T. (1998). Cenozoic erosion and the preglacial uplift of the Svalbard-Barents Sea region. *Tectonophysics*, *300*(1–4), 311–327. https://doi.org/10.1016/S0040-1951(98)00245-5

Dumas, S., & Arnott, R. W. C. (2006). Origin of hummocky and swaley cross-stratification—The controlling influence of unidirectional current strength and aggradation rate. *Geology*, *34*(12), 1073–1076. https://doi.org/10.1130/G22930A.1

Dypvik, H., Hakansson, E., & Heinberg, C. (2002). Jurassic and Cretaceous palaeogeography and stratigraphic comparisons in the North Greenland-Svalbard region. *Polar Research*, *21*, 91–108. https://doi.org/10.3402/polar.v21i1.6476

Edwards, M. B. (1976). Growth faults in Upper Triassic deltaic sediments. *Svalbard. AAPG Bulletin*, *60*(3), 341–355.

Eide, C. H., Klausen, T. G., Katkov, D., Suslova, A. A., & Helland-Hansen, W. (2017). Linking an Early Triassic delta to antecedent topography: Source-to-sink study of the southwestern Barents Sea margin. *Bulletin*, *130*(1–2), 263–283.

Faleide, J. I., Gudlaugsson, S. T., & Jacquart, G. (1984). Evolution of the western Barents Sea. *Marine and Petroleum Geology*, *1*(2), 123–150. https://doi.org/10.1016/0264-8172(84)90082-5

Faleide, J. I., Pease, V., Curtis, M., Klitzke, P., Minakov, A., Sheck-Wenderoth, M., … Zayonchek, A. (2017). Tectonic implications of the lithospheric structure across the Barents and Kara shelves. *Geological Society of London, Special Publications*, *460*, 285–314. https://doi.org/10.1144/SP460.18

Faleide, J. I., Tsikalas, F., Breivik, A. J., Mjelde, R., Ritzmann, O., Engen, Ø., … Eldholm, O. (2008). Structure and evolution of the continental margin off Norway and the Barents Sea. *Episodes*, *31*(1), 82–91. https://doi.org/10.18814/epiiugs/2008/v31i1/012

Fazlikhani, H., Back, S., Kukla, P. A., & Fossen, H. (2017). Interaction between gravity-driven listric normal fault linkage and their hanging-wall rollover development: A case study from the western Niger Delta, Nigeria. *Geological Society, London, Special Publications*, *439*(1), 169–186. https://doi.org/10.1144/SP439.20

Fielding, C. R. (2006). Upper flow regime sheets, lenses and scour fills: Extending the range of architectural elements for fluvial sediment bodies. *Sedimentary Geology*, *190*(1–4), 227–240. https://doi.org/10.1016/j.sedgeo.2006.05.009

Fielding, C. R. (2015). Anatomy of falling-stage deltas in the Turonian Ferron Sandstone of the western Henry Mountains Syncline, Utah: Growth faults, slope failures and mass transport complexes. *Sedimentology*, *62*(1), 1–26. https://doi.org/10.1111/sed.12136

Flood, B., Nagy, J., & Winsnes, T. S. (1971). The Triassic succession of Barentsøya, Edgeøya, and Hopen (Svalbard). *Norsk Polarinstitutt Meddelelser*, *100*, 1–20.

Garfunkel, Z. (1984). Large-scale submarine rotational slumps and growth faults in the eastern Mediterranean. *Marine Geology*, *55*(3–4), 305–324. https://doi.org/10.1016/0025-3227(84)90074-4

Gingras, M. K., Pemberton, S. G., & Smith, M. (2014). Bioturbation: Reworking sediments for better or worse. *Oilfield Review*, *26*(4), 46–58.

Gjelberg, J., & Steel, R. J. (1995). Helvetiafjellet Formation (Barremian–Aptian), Spitsbergen: Characteristics of a transgressive succession. In R. J. Steel, V. L. Felt, E. P. Johannessen, & C. Mathieu (Eds), *Sequence stratigraphy on the Northwest European Margin* (pp. 571–593). Amsterdam: Norwegian Petroleum Society (NPF) Special Publication 5, Elsevier.

Glørstad-Clark, E., Birkeland, E. P., Nystuen, J. P., Faleide, J. I., & Midtkandal, I. (2011). Triassic platform-margin deltas in the western Barents Sea. *Marine and Petroleum Geology*, *28*(7), 1294–1314. https://doi.org/10.1016/j.marpetgeo.2011.03.006

Glørstad-Clark, E., Faleide, J. I., Lundschien, B. A., & Nystuen, J. P. (2010). Triassic seismic sequence stratigraphy and paleogeography of the western Barents Sea area. *Marine and Petroleum Geology*, *27*(7), 1448–1475. https://doi.org/10.1016/j.marpetgeo.2010.02.008

Grundvåg, S. A., Marin, D., Kairanov, B., Śliwińska, K. K., Nøhr-Hansen, H., Jelby, M. E., … Olaussen, S. (2017). The Lower Cretaceous succession of the northwestern Barents Shelf: Onshore and offshore correlations. *Marine and Petroleum Geology*, *86*, 834–857. https://doi.org/10.1016/j.marpetgeo.2017.06.036

Grundvåg, S. A., & Olaussen, S. (2017). Sedimentology of the Lower Cretaceous at Kikutodden and Keilhaufjellet, southern Spitsbergen: Implications for an onshore–offshore link. *Polar Research*, *36*, 1. https://doi.org/10.1080/17518369.2017.1302124

Haile, B. G., Klausen, T. G., Czarniecka, U., Xi, K., Jahren, J., & Hellevang, H. (2018). How are diagenesis and reservoir quality linked to depositional facies? A deltaic succession, Edgeøya, Svalbard. *Marine and Petroleum Geology*, *92*, 519–546. https://doi.org/10.1016/j.marpetgeo.2017.11.019

Harland, W. B., & Kelly, S. R. A. (1997). Eastern svalbard platform. In W. B. Harland (Ed.), *The geology of svalbard* (Vol. *17*, pp. 75–95). London: Geological Society, Memoirs. https://doi.org/10.1144/GSL.MEM.1997.017.01.05

Henriksen, E., Bjørnseth, H. M., Hals, T. K., Heide, T., Kiryukhina, T., Kløvjan, O., … Sollid, K. (2011). Uplift and erosion of the greater Barents Sea: Impact on prospectivity and petroleum systems. *Geological Society, London, Memoirs*, *35*(1), 271–281.

Hiscott, R. N. (2001). Depositional sequences controlled by high rates of sediment supply, sea-level variations, and growth faulting: The Quaternary Baram Delta of northwestern Borneo. *Marine Geology*, *175*(1–4), 67–102. https://doi.org/10.1016/S0025-3227(01)00118-9

Høy, T., & Lundschien, B. A. (2011). Triassic deltaic sequences in the northern Barents Sea. *Geological Society, London, Memoirs*, *35*(1), 249–260.

Ings, S. J., & Beaumont, C. (2010). Shortening viscous pressure ridges, a solution to the enigma of initiating salt 'withdrawal' minibasins. *Geology*, *38*(4), 339–342.

Jelby, M. E., Grundvåg, S. A., Helland-Hansen, W., Olaussen, S., & Stemmerik, L. (2017). Basin-scale facies model of spectacular storm deposits in the High Arctic. Geological Society of Denmark Annual meeting 2017, Copenhagen, Denmark.

Johannessen, E. P., & Steel, R. J. (1992). Mid-Carboniferous extension and rift-infill sequences in the Billefjorden Trough, Svalbard. *Norsk Geologisk Tidsskrift*, *72*(1), 35–48.

Klausen, T. G., & Mørk, A. (2014). The upper triassic paralic deposits of the De Geerdalen formation on hopen: outcrop analog to the subsurface snadd formation in the barents sea the De Geerdalen formation on hopen. *AAPG Bulletin*, *98*(10), 1911–1941. https://doi.org/10.1306/02191413064

Klausen, T. G., Ryseth, A. E., Helland-Hansen, W., Gawthorpe, R., & Laursen, I. (2015). Regional development and sequence stratigraphy of the Middle to Late Triassic Snadd formation, Norwegian Barents Sea. *Marine and Petroleum Geology*, *62*, 102–122. https://doi.org/10.1016/j.marpetgeo.2015.02.004

Klausen, T. G., Torland, J. A., Eide, C. H., Alaei, B., Olaussen, S., & Chiarella, D. (2018). Clinoform development and topset evolution in a mud-rich delta–the Middle Triassic Kobbe Formation, Norwegian Barents Sea. *Sedimentology*, *65*(4), 1132–1169. https://doi.org/10.1111/sed.12417

Koevoets, M. J., Hammer, O., Olaussen, S., Senger, K., & Smelror, M. (2019). Integrating subsurface and outcrop data of the Middle Jurassic to Lower Cretaceous Agardhfjellet Formation in central Spitsbergen. *Norwegian Journal of Geology*, *98*, 1–34. https://doi.org/10.17850/njg98-4-01

Krajewski, K. P. (2008). The Botneheia Formation (Middle Triassic) in Edgeøya and Barentsøya, Svalbard: Lithostratigraphy, facies, phosphogenesis, paleoenvironment. *Polish Polar Research*, *29*(4), 319–364.

Longhitano, S. G., Mellere, D., Steel, R. J., & Ainsworth, R. B. (2012). Tidal depositional systems in the rock record: A review and new insights. *Sedimentary Geology*, *279*, 2–22. https://doi.org/10.1016/j.sedgeo.2012.03.024

Lopez, J. A. (1990). Structural styles of growth faults in the US Gulf Coast Basin. *Geological Society, London, Special Publications*, *50*(1), 203–219. https://doi.org/10.1144/GSL.SP.1990.050.01.10

López-Blanco, M., Marzo, M., & Muñoz, J. A. (2003). Low-amplitude, synsedimentary folding of a deltaic complex: Roda Sandstone (lower Eocene), South-Pyrenean Foreland Basin. *Basin Research*, *15*(1), 73–96. https://doi.org/10.1046/j.1365-2117.2003.00193.x

Lord, G. S., Johansen, S. K., Støen, S. J., & Mørk, A. (2017). Facies development of the Upper Triassic succession on Barentsøya, Wilhelmøya and NE Spitsbergen, Svalbard. *Norwegian Journal of Geology*, *97*(1). https://doi.org/10.17850/njg97-1-03

Lord, G. S., Solvi, K. H., Klausen, T. G., & Mørk, A. (2014). Triassic channel bodies on Hopen, Svalbard: Their facies, stratigraphical significance and spatial distribution. *Norwegian Petroleum Directorate Bulletin*, *11*, 41–59.

Lundschien, B. A., Høy, T., & Mørk, A. (2014). Triassic hydrocarbon potential in the Northern Barents Sea; integrating Svalbard and stratigraphic core data. *Norwegian Petroleum Directorate Bulletin*, *11*, 3–20.

Maher, H. D., Ogata, K., & Braathen, A. (2017). Cone-in-cone and beef mineralization associated with Triassic growth basin faulting and shallow shale diagenesis, Edgeøya, Svalbard. *Geological Magazine*, *154*(2), 201–216. https://doi.org/10.1017/S0016756815000886

Martinsen, O. J. (1989). Styles of soft-sediment deformation on a Namurian (Carboniferous) delta slope, Western Irish Namurian Basin, Ireland. *Geological Society, London, Special Publications*, *41*(1), 167–177. https://doi.org/10.1144/GSL.SP.1989.041.01.13

Martinsen, O. J., & Bakken, B. (1990). Extensional and compressional zones in slumps and slides in the Namurian of County Clare, Ireland. *Journal of the Geological Society*, *147*(1), 153–164. https://doi.org/10.1144/gsjgs.147.1.0153

Martinsen, O. J., Lien, T., Walker, R. G., & Collinson, J. D. (2003). Facies and sequential organisation of a mudstone-dominated slope and basin floor succession: The Gull Island Formation, Shannon Basin, Western Ireland. *Marine and Petroleum Geology*, *20*(6–8), 789–807. https://doi.org/10.1016/j.marpetgeo.2002.10.001

Massari, F. (1996). Upper-flow-regime stratification types on steep-face, coarse-grained, Gilbert-type progradational wedges (Pleistocene, southern Italy). *Journal of Sedimentary Research*, *66*(2), 364–375.

McClay, K. R., Dooley, T., & Lewis, G. (1998). Analog modeling of progradational delta systems. *Geology*, *26*(9), 771–774. https://doi.org/10.1130/0091-7613(1998)026<0771:AMOPDS>2.3.CO;2

Midtkandal, I., & Nystuen, J. P. (2009). Depositional architecture of alow-gradient ramp shelf in an epicontinental sea: The lower Cretaceous of Svalbard. *Basin Research*, *21*(5), 655–675. https://doi.org/10.1111/j.1365-2117.2009.00399.x

Midtkandal, I., Nystuen, J. P., Nagy, J., & Mørk, A. (2008). Lower Cretaceous lithostratigraphy across a regional subaerial unconformity in Spitsbergen: The Rurikfjellet and Helvetiafjellet formations. *Norwegian Journal of Geology*, *88*(4), 287–304.

Mørk, A., Dallmann, W. K., Dypvik, H., Johannessen, E. P., Larssen, G. B., Nagy, J., Nøttvedt, A. … Worsley, D. (1999) Mesozoic lithostratigraphy. In Lithostratigraphic lexicon of Svalbard. Upper Palaeozoic to Quaternary bedrock. Review and recommendations for nomenclature use (Ed. By: Dallmann, W. K.). *Tromsø, Norsk Polarinstitutt*,127–214.

Mørk, A., Knarud, R., & Worsley, D. (1982). Depositional and diagenetic environments of the Triassic and Lower Jurassic succession of Svalbard. In A. F. Embry, & H. R. Balkwill (Eds.), *Artic geology and geophysics: proceedings of the Third International Symposium on Arctic Geology Memoir* 8, (371–398) Calgary: Canadian Society of Petroleum Geologist.

Mørk, M. B. E. (1999). Compositional variations and provenance of Triassic sandstones from the Barents Shelf. *Journal of Sedimentary Research*, *69*(3), 690–710. https://doi.org/10.2110/jsr.69.690

Morley, C. K., Back, S., Van Rensbergen, P., Crevello, P., & Lambiase, J. J. (2003). Characteristics of repeated, detached, Miocene-Pliocene tectonic inversion events, in a large delta province on an active margin, Brunei Darussalam. *Borneo. Journal of Structural Geology*, *25*(7), 1147–1169. https://doi.org/10.1016/S0191-8141(02)00130-X

Morley, C. K., & Guerin, G. (1996). Comparison of gravity-driven deformation styles and behavior associated with mobile shales and salt. *Tectonics*, *15*(6), 1154–1170. https://doi.org/10.1029/96TC01416

Mulder, T., Syvitski, J. P., Migeon, S., Faugeres, J. C., & Savoye, B. (2003). Marine hyperpycnal flows: Initiation, behavior and related deposits. A Review. *Marine and Petroleum Geology*, *20*(6–8), 861–882. https://doi.org/10.1016/j.marpetgeo.2003.01.003

Mulrooney, M. J., Leutscher, J., & Braathen, A. (2017). A 3D structural analysis of the Goliat field, Barents Sea, Norway. *Marine and Petroleum Geology*, *86*, 192–212. https://doi.org/10.1016/j.marpetgeo.2017.05.038

Mulrooney, M. J., Rismyhr, B., Yenwongfai, H. D., Leutscher, J., Olaussen, S., & Braathen, A. (2018). Impacts of small-scale faults on continental to coastal plain deposition: Evidence from the Realgrunnen Subgroup in the Goliat field, southwest Barents Sea, Norway. *Marine and Petroleum Geology*, *95*, 276–302. https://doi.org/10.1016/j.marpetgeo.2018.04.023

Mutti, E. (1992). Turbidite sandstones. *AGIP, Istituto di geologia, Università di Parma, San Donato Milanese*, 275 pp.

Mutti, E., Tinterri, R., Benevelli, G., di Biase, D., & Cavanna, G. (2003). Deltaic, mixed and turbidite sedimentation of ancient foreland basins. *Marine and Petroleum Geology*, *20*(6–8), 733–755. https://doi.org/10.1016/j.marpetgeo.2003.09.001

Nemec, W., Steel, R. J., Gjelberg, J., Collinson, J. D., Prestholm, E., & Oxnevad, I. E. (1988). Anatomy of collapsed and re-established delta front in Lower Cretaceous of eastern Spitsbergen: Gravitational sliding and sedimentation processes. *AAPG Bulletin*, *72*(4), 454–476.

Nio, S. D., & Yang, C. S. (1991). Diagnostic attributes of clastic tidal deposits: A review. In Clastic Tidal Sedimentology (Ed. by D. G. Smith et al.). CSPG Special Publications, Clastic Tidal Sedimentology, Memoir 16. Mem can Soc Pet Geol, *16*, 3–27.

Ocamb, R. D. (1961). Growth faults of south Louisiana. *Transactions of the Gulf Coast Association of Geological Societies*, 139–174.

Ogata, K., Mulrooney, M. J., Braathen, A., Maher, H., Osmundsen, P. T., Anell, I., … Balsamo, F. (2018). Architecture, deformation style and petrophysical properties of growth fault systems: The Late Triassic deltaic succession of southern Edgeøya (East Svalbard). *Basin Research*, *30*(5), 1042–1073. https://doi.org/10.1111/bre.12296

Olariu, C., Steel, R. J., Dalrymple, R. W., & Gingras, M. K. (2012). Tidal dunes versus tidal bars: The sedimentological and architectural characteristics of compound dunes in a tidal seaway, the lower Baronia Sandstone (Lower Eocene), Ager Basin, Spain. *Sedimentary Geology*, *279*, 134–155. https://doi.org/10.1016/j.sedgeo.2012.07.018

Olariu, M. I., Olariu, C., Steel, R. J., Dalrymple, R. W., & Martinius, A. W. (2012). Anatomy of a laterally migrating tidal bar in front of a delta system: Esdolomada Member, Roda Formation, Tremp-Graus Basin, Spain. *Sedimentology*, *59*(2), 356–378. https://doi.org/10.1111/j.1365-3091.2011.01253.x

Olaussen, S., Larssen, G. B., Helland-Hansen, W., Johannessen, E. P., Nøttvedt, A., Riis, F., … Worsley, D. (2018). Mesozoic strata of the Kong Karls Land archipelago, Arctic Norway; a link to the northern Barents Sea basins. *Norwegian Journal of Geology*, *98*, 1–69.

Osmundsen, P. T., Braathen, A., Rød, R. S., & Hynne, I. B. (2014). Styles of normal faulting and fault-controlled sedimentation in the Triassic deposits of Eastern Svalbard. *Norwegian Petroleum Directorate Bulletin*, *11*, 61–79.

Owen, G. (1987). Deformation processes in unconsolidated sands. *Geological Society, London, Special Publications*, *29*(1), 11–24. https://doi.org/10.1144/GSL.SP.1987.029.01.02

Paterson, N. W., & Mangerud, G. (2015). Late Triassic (Carnian-Rhaetian) palynology of Hopen, Svalbard. *Review of Palaeobotany and Palynology*, *220*, 98–119. https://doi.org/10.1016/j.revpalbo.2015.05.001

Pickering, K., Stow, D., Watson, M., & Hiscott, R. (1986). Deep-water facies, processes and models: A review and classification scheme for modern and ancient sediments. *Earth-Science Reviews*, *23*(2), 75–174. https://doi.org/10.1016/0012-8252(86)90001-2

Potter, P. E., Maynard, J. B., & Depetris, P. J. (2005). Mud and mudstones: Introduction and overview. *Springer Science & Business Media*, 1–296.

Prestholm, E., & Walderhaug, O. (2000). Synsedimentary faulting in a Mesozoic deltaic sequence, Svalbard, Arctic Norway-Fault geometries, faulting mechanisms, and sealing properties. *AAPG Bulletin*, *84*(4), 505–522.

Riis, F., Lundschien, B. A., Høy, T., Mørk, A., & Mørk, M. B. E. (2008). Evolution of the Triassic shelf in the northern Barents Sea region. *Polar Research*, *27*(3), 318–338. https://doi.org/10.1111/j.1751-8369.2008.00086.x

Rismyhr, B., Bjærke, T., Olaussen, S., Mulrooney, M. J., & Senger, K. (2019). Facies, palynostratigraphy and sequence stratigraphy of the Wilhelmøya Subgroup (Upper Triassic-Middle Jurassic) in western central Spitsbergen, Svalbard. *Norsk Geologisk Tidsskrift*, *99*(4), 35–36. https://doi.org/10.17850/njg001

Rød, R. S., Hynne, I. B., & Mørk, A. (2014). Depositional environment of the Upper Triassic De Geerdalen Formation—an EW transect from Edgeøya to Central Spitsbergen, Svalbard. *Norwegian Petroleum Directorate Bulletin*, *11*, 21–40.

Röhnert, A. D. (2016). Geometry and sedimentary facies of low-angle clinoforms, Edgeøya, Svalbard. (Master's Thesis, duo.uio.no).

Rossi, V. M., Kim, W., Leva López, J., Edmonds, D., Geleynse, N., Olariu, C., … Passalacqua, P. (2016). Impact of tidal currents on delta-channel deepening, stratigraphic architecture, and sediment bypass beyond the shoreline. *Geology*, *44*(11), 927–930. https://doi.org/10.1130/G38334.1

Rossi, V. M., Longhitano, S. G., Mellere, D., Dalrymple, R. W., Steel, R. J., Chiarella, D., & Olariu, C. (2017). Interplay of tidal and fluvial processes in an early Pleistocene, delta-fed, strait margin (Calabria, Southern Italy). *Marine and Petroleum Geology*, *87*, 14–30. https://doi.org/10.1016/j.marpetgeo.2017.02.021

Rossi, V. M., & Steel, R. J. (2016). The role of tidal, wave and river currents in the evolution of mixed-energy deltas: Example from the Lajas Formation (Argentina). *Sedimentology*, *63*(4), 824–864. https://doi.org/10.1111/sed.12240

Rotevatn, A., & Jackson, C. A. L. (2014). 3D structure and evolution of folds during normal fault dip linkage. *Journal of the Geological Society*, *171*(6), 821–829. https://doi.org/10.1144/jgs2014-045

Rouby, D., Nalpas, T., Jermannaud, P., Robin, C., Guillocheau, F., & Raillard, S. (2011). Gravity driven deformation controlled by the migration of the delta front: The Plio-Pleistocene of the Eastern Niger Delta. *Tectonophysics*, *513*(1–4), 54–67. https://doi.org/10.1016/j.tecto.2011.09.026

Rykkelid, E., & Fossen, H. (2002). Layer rotation around vertical fault overlap zones: Observations from seismic data, field examples, and physical experiments. *Marine and Petroleum Geology*, *19*(2), 181–192. https://doi.org/10.1016/S0264-8172(02)00007-7

Ryseth, A. (2014). Sedimentation at the Jurassic-Triassic boundary, south-west Barents Sea. In A. W. Martinius, R. Ravnås, J. A. Howell, R. J. Steel, & J. P. Wonham (Eds.), *From Depositional Systems to Sedimentary Successions on the Norwegian Continental Margin* (187–214). Egham, UK: International Association of Sedimentologists Special Publication.

Seilacher, A. (1991). Events and their signatures—an overview. *Cycles and Events in Stratigraphy*, 222–226.

Serck, C. S., & Braathen, A. (2019). Extensional fault and fold growth: Impact on accommodation evolution and sedimentary infill. *Basin Research*, *31*(5), 967–990. https://doi.org/10.1111/bre.12353

Serck, C. S., Faleide, J. I., Braathen, A., Kjølhamar, B., & Escalona, A. (2017). Jurassic to early cretaceous basin configuration (s) in the Fingerdjupet Subbasin, SW Barents Sea. *Marine and Petroleum Geology*, *86*, 874–891. https://doi.org/10.1016/j.marpetgeo.2017.06.044

Shultz, M. R., & Hubbard, S. M. (2005). Sedimentology, stratigraphic architecture, and ichnology of gravity-flow deposits partially ponded in a growth-fault-controlled slope minibasin, Tres Pasos Formation (Cretaceous), southern Chile. *Journal of Sedimentary Research*, *75*(3), 440–453. https://doi.org/10.2110/jsr.2005.034

Smelror, M., Larssen, G. B., Olaussen, S., Rømuld, A., & Robert, W. (2018). Late Triassic to Early Cretaceous palynostratigraphy of Kong Karls Land, Svalbard. *Arctic Norway. Norwegian Journal of Geology*, *98*, 1–31. https://doi.org/10.17850/njg004

Smyrak-Sikora, A., Johannessen, E. P., Olaussen, S., Sandal, G., & Braathen, A. (2019). Sedimentary architecture during Carboniferous rift initiation–the arid Billefjorden Trough, Svalbard. *Journal of the Geological Society*, *176*(2), 225–252. https://doi.org/10.1144/jgs2018-100

Steel, R. J., & Worsley, D. (1984). Svalbard's post-Caledonian strata—an atlas of sedimentational patterns and palaeogeographic evolution In A. M. Spencer (Ed.), *Petroleum geology of the North European margin* (pp. 109–135). Dordrecht: Springer.

Taylor, A. M., & Goldring, R. (1993). Description and analysis of bioturbation and ichnofabric. *Journal of the Geological Society*, *150*(1), 141–148.

Taylor, S. K., Nicol, A., & Walsh, J. J. (2008). Displacement loss on growth faults due to sediment compaction. *Journal of Structural Geology*, *30*(3), 394–405. https://doi.org/10.1016/j.jsg.2007.11.006

Thomas, R. G., Smith, D. G., Wood, J. M., Visser, J., Calverley-Range, E. A., & Koster, E. H. (1987). Inclined heterolithic stratification—terminology, description, interpretation and significance. *Sedimentary Geology*, *53*(1–2), 123–179. https://doi.org/10.1016/S0037-0738(87)80006-4

Turner, B. R. (1981). Possible origin of low angle cross-strata and horizontal lamination in Beaufort group sandstones of the Southern Karoo Basins. *South African Journal of Geology*, *84*(3), 193–197.

Tvedt, A. B., Rotevatn, A., & Jackson, C. A. (2016). Supra-salt normal fault growth during the rise and fall of a diapir: Perspectives from 3D seismic reflection data, Norwegian North Sea. *Journal of Structural Geology*, *91*, 1–26. https://doi.org/10.1016/j.jsg.2016.08.001

Tvedt, A. B., Rotevatn, A., Jackson, C. A. L., Fossen, H., & Gawthorpe, R. L. (2013). Growth of normal faults in multilayer sequences: A 3D seismic case study from the Egersund Basin, Norwegian North Sea. *Journal of Structural Geology*, *55*, 1–20. https://doi.org/10.1016/j.jsg.2013.08.002

van der Zee, W., & Urai, J. L. (2005). Processes of normal fault evolution in a siliciclastic sequence: A case study from Miri, Sarawak, Malaysia. *Journal of Structural Geology*, *27*(12), 2281–2300. https://doi.org/10.1016/j.jsg.2005.07.006

Van Rensbergen, P., & Morley, C. K. (2000). 3D seismic study of a shale expulsion syncline at the base of the Champion delta, offshore Brunei and its implications for the early structural evolution of large delta systems. *Marine and Petroleum Geology*, *17*(8), 861–872. https://doi.org/10.1016/S0264-8172(00)00026-X

Van Wagoner, J. C., Posamentier, H. W., Mitchum, R. M., Vail, P. R., Sarg, J. F., Loutit, T. S., & Hardenbol, J., (1988). An overview of the fundamentals of sequence stratigraphy and key definitions. In: Sea-Levels Changes—an Integrated Approach (Ed by: Wilgus, C.K., Posamenier, H., Ross, C. A. & . Kendall, C. G. St. C). *Society of Economic Paleontologists and Mineralogists Special Publication*, *42*, 39–45.

Venditti, J. G., Church, M., & Bennett, S. J. (2005). On the transition between 2D and 3D dunes. *Sedimentology*, *52*(6), 1343–1359. https://doi.org/10.1111/j.1365-3091.2005.00748.x

Vigran, J. O., Mangerud, G., Mørk, A., Worsley, D., & Hochuli, P. (2014). Palynology and geology of the Triassic succession of Svalbard and the Barents Sea. *Geological Survey of Norway Special Publication*, *14*, 1–270.

Visser, M. J. (1980). Neap-spring cycles reflected in Holocene subtidal large-scale bedform deposits: A preliminary note. *Geology*, *8*(11), 543–546. https://doi.org/10.1130/0091-7613(1980)8<543:NCRIHS>2.0.CO;2

Walker, R. G. (1992). Facies, facies models and modern stratigraphic concepts. In R. G. Walker & N. P. James (Eds.), *Facies models: Response to sea-level change* (pp. 1–14). Newfoundland, Canada: Geological Association of Canada.

Walsh, J. J., Bailey, W. R., Childs, C., Nicol, A., & Bonson, C. G. (2003). Formation of segmented normal faults: A 3-D perspective. *Journal*

of Structural Geology, *25*(8), 1251–1262. https://doi.org/10.1016/S0191-8141(02)00161-X

Weber, K. J. (1987). Hydrocarbon distribution patterns in Nigerian growth fault structures controlled by structural style and stratigraphy. *Journal of Petroleum Science and Engineering*, *1*(2), 91–104. https://doi.org/10.1016/0920-4105(87)90001-5

Wignall, P. B., & Best, J. L. (2004). Sedimentology and kinematics of a large, retrogressive growth-fault system in Upper Carboniferous deltaic sediments, western Ireland. *Sedimentology*, *51*(6), 1343–1358. https://doi.org/10.1111/j.1365-3091.2004.00673.x

Willis, B. J. (2005). Deposits of tide-influenced river deltas. In: River Deltas- Concepts, Models, and Examples SEPM Special Publication No.83 pp. 87–129.

Winker, C. D., & Edwards, M. B. (1983). Unstable progradational clastic shelf margins. Special Publications of SEPM, Vol. 33 pp.139–157.

Worsley, D. (2008). The post-Caledonian development of Svalbard and the western Barents Sea. *Polar Research*, *27*(3), 298–317. https://doi.org/10.1111/j.1751-8369.2008.00085.x

Zecchin, M., Massari, F., Mellere, D., & Prosser, G. (2004). Anatomy and evolution of a Mediterranean-type fault bounded basin: The Lower Pliocene of the northern Crotone Basin (Southern Italy). *Basin Research*, *16*(1), 117–143. https://doi.org/10.1111/j.1365-2117.2004.00225.x

SUPPORTING INFORMATION

Additional supporting information may be found online in the Supporting Information section at the end of the article.

How to cite this article: Smyrak-Sikora A, Osmundsen PT, Braathen A, et al. Architecture of growth basins in a tidally influenced, prodelta to delta-front setting: The Triassic succession of Kvalpynten, East Svalbard. *Basin Res*. 2020;32:949–978. https://doi.org/10.1111/bre.12410